Research Square

Preprints are preliminary reports that have not undergone peer review.
They should not be considered conclusive, used to inform clinical practice,
or referenced by the media as validated information.

Sterol Remodeling in Fusarium oxysporum Drives Mammalian Virulence through Pyroptosis and Chemokine Suppression

Neta Shlezinger

neta.shlezinger1@mail.huji.ac.il

The Hebrew University https://orcid.org/0000-0003-0005-0756

Marina Rocha

Koret School of Veterinary Medicine, The Robert H. Smith Faculty of Agricultural, Food & Environment, The Hebrew University of Jerusalem https://orcid.org/0000-0003-4988-7629

John Adeoye

The Hebrew University

Hilla Hayby

The Hebrew University

Siyuan Wu

University of Massachusetts https://orcid.org/0000-0002-6211-5810

Evandro Ortigossa

Weizmann Institute of Science

Enrico Garbe

Research Group (Epi-)Genetic Regulation of Fungal Virulence, Leibniz Institute for Natural Product Research and Infection Biology- Hans-Knöll-Institute, Jena, Germany

Slavica Janevska

Leibniz Institute for Natural Product Research and Infection Biology-Hans Knöll Institute (Leibniz-HKI) https://orcid.org/0000-0001-7361-495X

Jeffrey Coleman

Auburn University https://orcid.org/0000-0001-8579-1996

Li-Ju Ma

University of Massachusetts

Article

Keywords:

Posted Date: April 1st, 2026

DOI: https://doi.org/10.21203/rs.3.rs-9124666/v1

License: This work is licensed under a Creative Commons Attribution 4.0 International License.
Read Full License

Additional Declarations: There is **NO** Competing Interest.

Sterol Remodeling in *Fusarium oxysporum* Drives Mammalian Virulence through Pyroptosis and Chemokine Suppression

Authors list: Marina Campos Rocha[1], John Adeoye[1], Hilla Hayby[1], Melanie Wu[2], Evandro S. Ortigossa[3], Enrico Garbe[4,5], Slavica Janevska[4], Jeffrey J. Coleman[6], Li-Ju Ma[2], Neta Shlezinger[1]

Affiliations:

[1]Koret School of Veterinary Medicine, Faculty of Agriculture, The Hebrew University, Rehovot, Israel

[2]Department of Biochemistry and Molecular Biology, University of Massachusetts Amherst, Amherst, MA, USA. Molecular and Cellular Biology Graduate Program, University of Massachusetts Amherst, Amherst, MA, USA

[3]Department of Computer Science and Applied Mathematics, Weizmann Institute of Science, Rehovot, Israel

[4](Epi-)Genetic Regulation of Fungal Virulence, Leibniz Institute for Natural Product Research and Infection Biology-Hans Knöll Institute (Leibniz-HKI), Jena, Germany

[5]National Reference Center for Invasive Fungal Infections, Leibniz Institute for Natural Product Research and Infection Biology-Hans Knöll Institute (Leibniz-HKI), Jena, Germany

[6]Department of Entomology and Plant Pathology, Auburn University, Auburn, AL 36849, USA

Corresponding author: neta.shlezinger1@mail.huji.ac.il

Keywords:

ABSTRACT

Members of the *Fusarium oxysporum* species complex are globally distributed soil fungi and plant pathogens that increasingly cause severe and often treatment-refractory human infections. Because clinical and non-clinical isolates arise from overlapping ecological reservoirs, the biological features that contribute to enhanced virulence in mammalian hosts remain

incompletely defined. Here, we identify remodeling of ergosterol homeostasis as a distinguishing characteristic of clinically derived isolates, which displayed increased ergosterol biosynthetic activity, elevated extracellular ergosterol release, reduced azole accumulation, and increased pathogenicity in a murine infection model. Functionally, heightened sterol flux promoted caspase-1–dependent macrophage pyroptosis while selectively suppressing chemokine production through IL-10/TGF-β–associated pathways, resulting in impaired neutrophil recruitment despite robust proinflammatory cytokine induction. We propose that enhanced sterol biosynthesis, potentially favored under azole exposure, amplifies pathogenic potential in mammalian hosts. These findings redefine ergosterol as an immunomodulatory virulence determinant linking sterol metabolism, host adaptation, and disease severity.

Main Text

Infections caused by fungi represent a massive global health burden, with estimates suggesting that over one billion people are affected and approximately 1.6 million die annually[1]. Unlike obligate human pathogens, the primary agents responsible for invasive mycoses are environmental opportunists that circulate through soil, water, and the built environment, including hospital infrastructure, inducing disease when host defenses and immune regulation are compromised[1]. The growing population of immunocompromised patients, together with sustained environmental exposure, is transforming the clinical landscape and exposing enduring gaps in diagnosis, antifungal treatment, and infection prevention. Within the broader rise of opportunistic mycoses, a significant development is the growing awareness of fungi that infect both plants and animals, including humans, blurring the traditional boundary between agricultural and medical mycology[2,3]. This environmental origin means that these organisms are not inherently adapted to the human host; instead, they may acquire their pathogenic potential through an "environmental virulence school"[4]. Traits developed through exposure to diverse environmental biotic and abiotic pressures, such as stress resilience, tissue invasion, and nutrient acquisition, can be adapted for survival and pathogenicity in mammals[5]. This dual-threat phenomenon is exemplified by *Fusarium* species. Known primarily as one of the top five most significant plant pathogens, they are increasingly recognized as serious opportunistic pathogens in humans and have been classified as high-priority fungal pathogens by the World Health Organization[6–8]. Although there is a detailed understanding of the genomic features that drive host specificity in plant infections, the characteristics that enable environmental fungi to evade immune defenses and cause fatal disease in mammals remain poorly understood.

This gap is especially significant for the *F. oxysporum* species complex (FOSC), which presents increasing challenges for both agriculture and medicine. Traditionally known as the cause of vascular wilt in over 100 crop species[9], *Fusarium ssp.* also ranks as a leading cause of fungal keratitis and an important cause of invasive fusariosis in humans[10–12]. This is particularly true for immunocompromised patients with hematologic malignancies, in whom mortality rates can approach 100% despite antifungal therapy[13]. Its inclusion on the WHO Fungal Priority Pathogens List highlights the urgency of identifying factors that contribute to human adaptation

of environmentally acquired pathogens and adverse clinical outcomes[14]. Adding to this concern, many *Fusarium* isolates exhibit inherent resistance or reduced susceptibility across multiple antifungal classes[15,16]. The widespread use of azole demethylase inhibitors in agriculture has also been proposed as a contributing factor to azole resistance in the FOSC[17].

Opportunistic fungal pathogens are typically acquired from environmental reservoirs and do not depend on mammalian hosts for survival or transmission. Instead, disease arises when environmental exposure coincides with host susceptibility. For an environmental microbe to establish infection in a mammalian host, it must withstand a series of physiological and immunological constraints distinct from those encountered in many environmental niches. While thermotolerance is a prerequisite for survival in the mammalian host, it alone is insufficient to explain virulence, as many environmental fungi capable of growth at mammalian temperatures rarely cause invasive disease[18]. Beyond temperature, invading microbes face a highly hostile host environment shaped by multilayered innate defense mechanisms[19]. These include physical barriers such as mucus and epithelial integrity[20]; chemical stresses such as acidic pH, antimicrobial peptides, oxidative stress, and hypoxia[21]; and nutritional immunity mechanisms that restrict access to essential metals or actively intoxicate pathogens within phagolysosomal compartments[22]. In parallel, cellular immunity mediated by macrophages, neutrophils, and other innate immune cells acts to detect, contain, and eliminate invading fungi[23]. Collectively, these pressures impose a formidable selective landscape that environmental microbes are not presumed to be specifically adapted to navigate. This raises a fundamental question in opportunistic mycology: are isolates recovered from clinical infections functionally distinct from those persisting in non-clinical ecological reservoirs, or do infections primarily reflect stochastic encounters between hosts and broadly adapted microbes? While the concept of an "environmental virulence school" proposes that traits selected under diverse ecological pressures, such as stress resistance, metabolic flexibility, and competitive fitness, may incidentally enhance pathogenicity in mammals, direct experimental evidence linking isolate origin to mammalian virulence remains limited. In particular, it remains unclear whether isolates recovered from clinical infections differ functionally from those persisting in non-clinical ecological reservoirs in their capacity to withstand immune attack, modulate host responses, or cause disease. These questions are especially relevant for *F. oxysporum*, a species complex comprising lineages capable of infecting plants, animals, and humans, reflecting its cross-

kingdom pathogenic capacity[24]. Despite extensive work on plant pathogenicity and host specificity within the FOSC, and recent reports describing distinct genomic features and increased thermotolerance in clinical isolates, comparatively little is known about the determinants of virulence in mammals. Importantly, because both clinical and non-clinical isolates of the FOSC ultimately originate from diverse environmental niches, including soil, plant-associated habitats, water systems, and built environments, whether clinical isolates represent bona fide mammalian-adapted lineages remains unclear. Rather, pathogenicity may emerge from traits selected under distinct ecological pressures that incidentally confer fitness within mammalian tissues. However, we still lack a systematic test of whether clinical FOSC isolates are inherently more virulent in mammals or whether they achieve pathogenicity through distinct strategies that modulate or evade host immunity.

Innate immune cells, particularly macrophages, play a central role in the early control of invasive fungal infections, including fusariosis, by sensing pathogen-associated molecular patterns and viability signals, producing inflammatory mediators, and coordinating neutrophil recruitment through chemokine secretion. Inflammasome activation, including signaling through the NLRP3 inflammasome, has emerged as a key pathway in antifungal immunity, linking detection of fungal-derived danger signals to maturation of IL-1β and induction of inflammatory cell death via pyroptosis[25,26]. While inflammasome activation can enhance fungal clearance in some contexts, excessive or premature activation may be detrimental, leading to loss of sentinel immune cells and disruption of coordinated cellular recruitment. For *F. oxysporum*, host immune responses have been described primarily at the level of cytokine induction and inflammatory pathology[27], but the extent to which different isolates differentially engage inflammasome pathways or induce inflammatory cell death remains poorly defined.

In this study, *F. oxysporum* isolates that were recovered from clinical infections were compared with non-clinically derived isolates in a murine model of fusariosis and characterized for isolate-associated differences in host immune responses and pathogenic traits. We show that clinically derived isolates display increased virulence and heightened leukocyte cytotoxicity. Mechanistically, we identify macrophage pyroptosis induction as a previously unrecognized outcome of *F. oxysporum* infection and demonstrate that clinically derived isolates elicit a distinctive immune response characterized by robust pro-inflammatory signaling coupled with

suppression of cellular recruitment. These effects are mediated, at least in part, by increased ergosterol production and secretion, linking fungal sterol metabolism to immune dysregulation and disease severity in mammalian hosts.

Results

Enhanced virulence of clinical *F. oxysporum* isolates is associated with inflammatory dysregulation and impaired cellular recruitment

To assess potential differences in pathogenicity between clinically and non-clinically derived *F. oxysporum* isolates, we compared the virulence of two clinical isolates—MRL8996[28] recovered from a patient with keratitis (hereafter referred to as the 'keratitis strain'), and NRRL3293[29], isolated from a blood culture of a leukemia patient (the 'blood strain')—with the well-characterized plant-derived strain *F. oxysporum* f. sp. *lycopersici* Fol4287 (the 'plant strain')[30]. To evaluate virulence in vivo, we employed an immunosuppressed murine model of fusariosis and compared disease progression following infection with the keratitis strain, the blood strain, or the plant strain.

Cyclophosphamide-treated C57BL/6JOlaHsd mice were inoculated intravenously with 10^6 microconidia, and survival was assessed over 10 days. Infection with both clinical isolates resulted in significantly increased mortality compared to the plant strain, although the kinetics and extent of lethality differed between isolates. Mice infected with the blood strain reached 100% mortality by day 7 post-infection, whereas infection with the keratitis strain resulted in approximately 80% mortality by the experimental endpoint. In contrast, mice challenged with the plant strain exhibited significantly prolonged survival, with ~50% of animals surviving to day 10 (Fig. 1a). These data demonstrate that while the plant strain retains the capacity to cause systemic disease in immunocompromised hosts, clinically recovered *F. oxysporum* isolates display markedly enhanced virulence in a murine model of disseminated fusariosis.

Beyond differences in survival, infection with plant- and clinically derived *F. oxysporum* isolates also resulted in strikingly distinct patterns of fungal burden, tissue pathology, and immune cell recruitment in vivo (Fig. 1b–i; Fig. S1). Systemic dissemination was evident in all infection groups, with fungal burden detectable in multiple organs as early as 2 days post-infection (dpi) and persisting through 5 dpi (Fig. 1b,c; Fig. S1a,b). At 2 dpi, CFU analysis demonstrated

increased fungal recovery in mice infected with both clinical strains compared to the plant strain across multiple organs (Fig. 1b). The blood and keratitis strains exhibited comparable burdens in the liver, while the blood strain showed modestly higher CFU counts in the lungs and heart. qPCR quantification revealed significantly elevated fungal DNA levels in mice infected with the blood strain, consistent with the overall trend of increased early dissemination among clinical isolates. At 5 dpi, viable fungi remained detectable in all examined organs across infection groups, indicating sustained systemic infection. Clear strain-dependent differences were evident at this stage, with the blood strain exhibiting the highest fungal burden across organs, followed by the keratitis strain, while the plant strain consistently showed the lowest CFU recovery (Fig. 1c). Notably, splenic fungal DNA levels increased between 2 and 5 dpi in mice infected with the blood strain, as determined by qPCR (Fig. S1a,b), whereas splenic CFU counts showed a slight reduction over the same interval. Although CFU counts were modestly reduced compared to 2 dpi in several organs, the overall kinetic profile, characterized by rapid dissemination followed by sustained organ colonization, is consistent with established models of systemic fungal infection.

Given that strain-dependent differences in fungal burden were most pronounced in the spleen at 5 dpi, we next examined splenic histopathology to assess the corresponding inflammatory response. Histopathological analysis of spleens collected 5 dpi revealed marked differences in inflammatory architecture between groups. Hematoxylin and eosin staining of spleens from mice infected with the plant strain showed extensive cellular infiltrates, characterized by dense accumulations of inflammatory cells that disrupted normal splenic organization (Fig. 1d). Consistent with this inflammatory expansion, spleens from mice infected with the plant strain were significantly enlarged compared to those from mice infected with clinical strains (Fig. 1e).

In contrast, spleens from mice infected with the clinical strains, despite exhibiting higher fungal burdens at this time point, largely retained their gross architecture but appeared markedly hypocellular, with sparse inflammatory infiltrates (Fig. 1d). Immunohistochemical staining for myeloperoxidase (MPO) confirmed a pronounced reduction in neutrophil presence in spleens from mice infected with the clinical strains compared to the plant strain (Fig. S1g), corroborating the reduced inflammatory cellularity observed by H&E staining.

Local pathology at the site of inoculation further highlighted differences between the plant and the clinical strains. At 10 dpi, neutropenic mice infected with either clinical strain developed extensive lesions at the tail vein injection site, characterized by prominent subcutaneous nodules and tissue damage (Fig. S1h). This pathology resembles the thrombosis and necrosis reported in other neutropenic fusariosis models[31]. Microscopic examination revealed invasive growth of dense septate hyphae extending into the dermis and subcutaneous tissue, accompanied by clusters of thick-walled spherical fungal cells consistent with chlamydospore-like structures in lesions caused by both clinical strains (Fig. S1h). Such invasive and necrotic pathology was not observed in mice infected with the plant strain.

To quantitatively assess immune cell recruitment, we performed flow cytometric analysis of leukocytes isolated from spleens and kidneys, gating on CD45+ cells and enumerating major innate immune populations. At 2 dpi, mice infected with the plant strain showed increased total leukocyte numbers in both organs compared with mice infected with the clinical strains (Fig. 1f,h). By 5 dpi, these differences became more pronounced, as infection with the plant strain induced robust leukocyte accumulation in both the spleen and the kidney, with marked increases in neutrophils, monocytes/macrophages, and dendritic cells (Fig. 1g,i).

In contrast, kidneys and spleens from mice infected with clinical strains showed minimal leukocyte expansion at 5 dpi, with mice infected with the blood strain exhibiting the most severe reduction in immune cell numbers, and mice infected with the keratitis strain displaying an intermediate phenotype (Fig. 1g).

Collectively, these data demonstrate that clinically derived *F. oxysporum* isolates cause more extensive tissue invasion and fungal dissemination while eliciting markedly reduced recruitment of innate immune cells to infected organs, in contrast to the plant-derived strain, which triggers substantial inflammatory cell accumulation associated with prolonged survival.

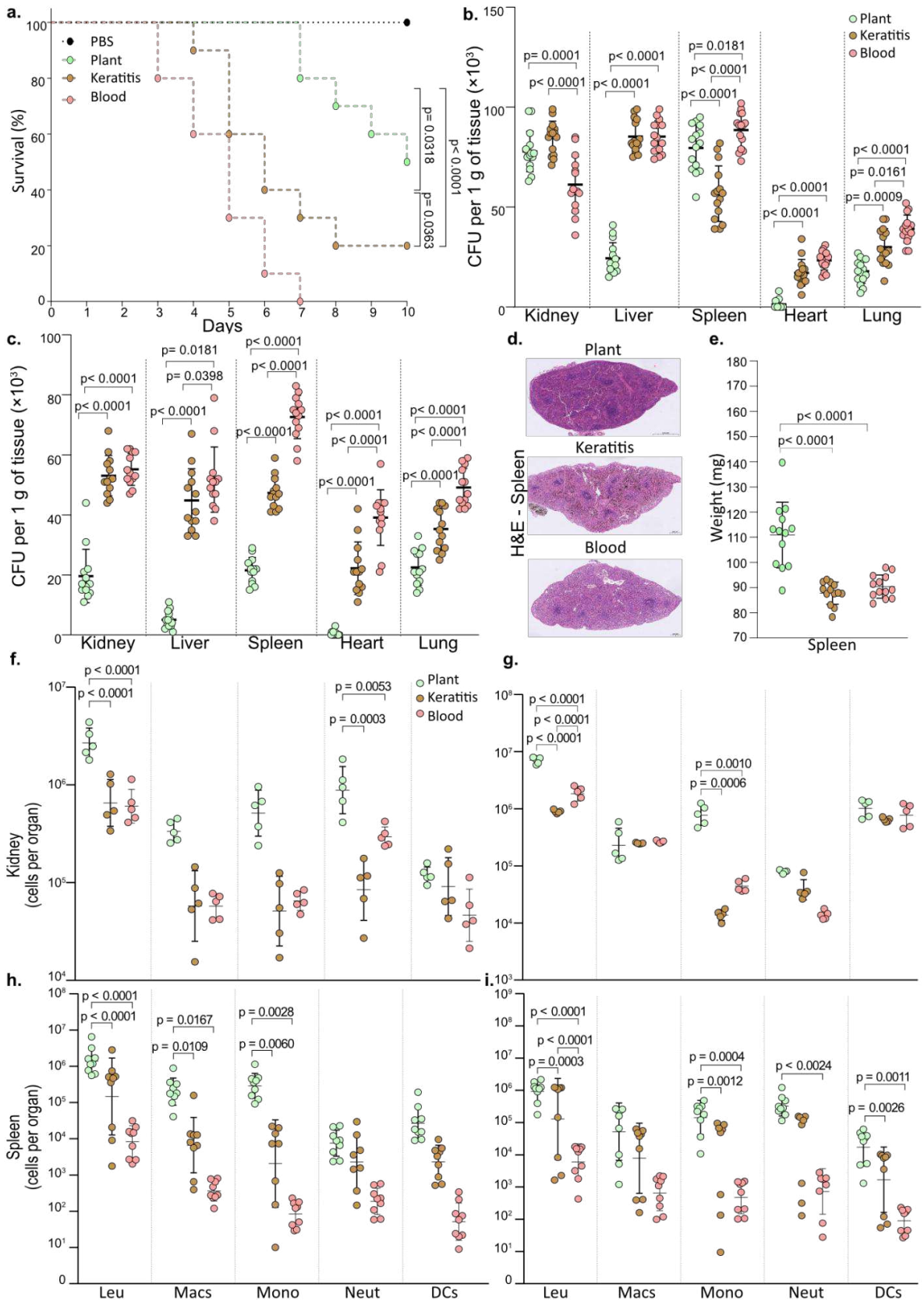
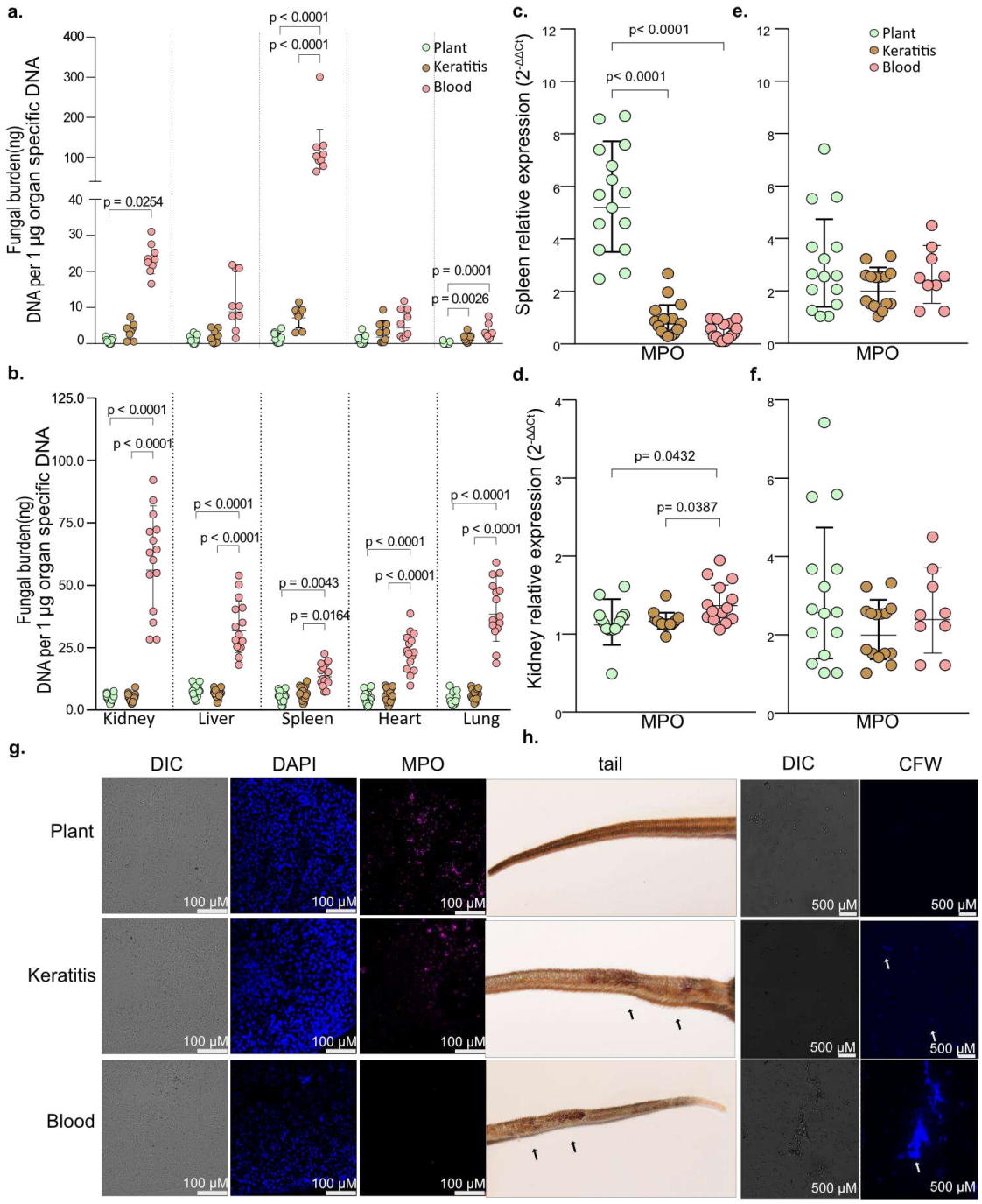

a.
PBS
Plant
Keratitis
Blood
Survival (%)
Days
p= 0.0318
p< 0.0001
p= 0.0363
b.
Plant
Keratitis
Blood
CFU per 1 g of tissue (×10³)
Kidney
Liver
Spleen
Heart
Lung
c.
CFU per 1 g of tissue (×10³)
Kidney
Liver
Spleen
Heart
Lung
d.
Plant
Keratitis
Blood
H&E - Spleen
e.
Weight (mg)
Spleen
f.
Plant
Keratitis
Blood
Kidney (cells per organ)
g.
h.
Spleen (cells per organ)
Leu
Macs
Mono
Neut
DCs
i.
Leu
Macs
Mono
Neut
DCs

Figure 1: Clinical *F. oxysporum* strains exhibit enhanced virulence and attenuated leukocyte recruitment relative to the plant strain. (a) Survival kinetics of cyclophosphamide-treated C57BL/6JOlaHsd mice (n=10 per group) following intravenous challenge with 1×10^6 microconidia of the plant (Fol4287) strain and clinical isolates (MRL8996 - keratitis, NRRL32931-blood), or PBS vehicle. (b,c) Fungal burden quantified by colony-forming units (CFU) in the kidney, liver, spleen, heart, and lung at 2 dpi (b) and 5 dpi (c) following intravenous inoculation with the plant-derived strain Fol4287 or the clinical isolates MRL8996 and NRRL32931. Data are expressed as CFU per gram of tissue ($\times10^3$). (d) Representative H&E staining of splenic architecture at 5 dpi. (e) Spleen weights recorded at necropsy (5 dpi). Data represent mean ± s.d. (f–i). Absolute quantification of innate immune cell populations in the kidney (f, g) and spleen (h, i) at 2 dpi (f, h) and 5 dpi (g, i). Populations were gated from total CD45+ leukocytes, and include macrophages, monocytes, neutrophils, and dendritic cells (DCs). Absolute cell numbers were derived from total organ cell counts. In d–i, each dot represents an individual mouse. Statistical analysis: (a) log-rank (Mantel–Cox); (c-i) one-way ANOVA with Tukey's multiple comparisons test; Data indicate mean ± s.e.m.



238

239 **Figure S1: Differential fungal burden and MPO responses accompany infection with**
240 **clinical versus plant *F. oxysporum* strains.** (a,b) Fungal burden quantified by qPCR in the
241 kidney, liver, spleen, heart, and lung at 2 dpi (a) and 5 dpi (b, expressed as ng fungal DNA per 1
242 µg organ DNA. (c–f) RT–qPCR analysis of *MPO* transcript levels in the spleen (c,e) and kidney

(d, f) at 2 dpi (c, d) and 5 dpi (e, f). Data are shown as relative expression ($2^{-\Delta\Delta ct}$), normalized to *ACTβ* and relative to uninfected animals. (g) Representative spleen architecture at 5 dpi visualized by differential interference contrast (DIC) and immunofluorescence microscopy. Sections were stained for nuclei (DAPI, blue) and myeloperoxidase (MPO, magenta). (h) Representative tail pathology at 10 dpi in cyclophosphamide-treated C57BL/6JOlaHsd mice following intravenous challenge with 10^6 microconidia. Left, macroscopic appearance showing localized swelling and necrotic lesions (arrows); middle, bright-field images of corresponding histological sections; right, calcofluor white (CFW) staining identifying fungal structures within the tissue (arrows). In a–f, each dot represents an individual mouse. Statistical analysis: (a-f) one-way ANOVA with Tukey's multiple comparisons test; Data indicate mean ± s.e.m.

An effective antifungal immune response is initiated by pathogen recognition, followed by the rapid induction of pro-inflammatory cytokines and chemokines that promote recruitment and activation of neutrophils and inflammatory monocytes[32]. These early responses are critical for restricting fungal proliferation by limiting conidial germination and hyphal outgrowth. To determine whether isolates associated with invasive human infection elicit distinct inflammatory programs, cytokine and chemokine responses were quantified in infected tissues using targeted qPCR and ELISA. At 2 dpi, analysis of cytokine and chemokine expression in the spleen revealed a clear divergence between the plant and the clinical strains (Fig. 2a). Infection with the clinical strains induced significantly higher expression of multiple pro-inflammatory and regulatory cytokines, including *IL-6*, *TNF*, *IL-18*, *IL-10*, and *TGF-β*, compared with infection with the plant strain. In contrast, expression of neutrophil-recruiting chemokines was largely comparable between isolates at this early systemic time point. A similar pattern was observed in the kidney at 2 dpi (Fig. 2b). Kidneys from mice infected with the clinical strains exhibited elevated expression of *IL-6*, *IL-1β*, *IL-18*, *IL-10*, and *TGF-β* relative to mice infected with the plant strain. Notably, *TNF* expression was not increased in the kidney at this time point, highlighting tissue-specific differences in cytokine induction. As in the spleen, chemokine expression at 2 dpi was broadly comparable between isolates, indicating that early differences were driven primarily by cytokine rather than chemokine responses.

Notably, *IL-18* expression closely mirrored that of *IL-1β* in the kidney at 2 dpi, with both transcripts significantly elevated in mice infected with the clinical strains compared to the plant

(Fig. 2b). In the spleen at this early time point, *IL-18*, but not *IL-1β*, was selectively increased in response to the clinical strains (Fig. 2a). *IL-1β* and *IL-18* are hallmark cytokines of inflammasome-associated inflammatory responses, as their maturation requires caspase-1–dependent processing[33]. The preferential induction of these cytokines, particularly within infected organs, indicates enhanced engagement of inflammasome-linked inflammatory pathways during infection with the clinical strains, distinguishing them from the plant strain.

By 5 dpi, these isolate-dependent differences became more pronounced and extended to chemokine expression. In the spleen, mice infected with the clinical isolates maintained elevated expression of inflammatory and regulatory cytokines, mirroring the pattern observed at 2 dpi (Fig. 2c). In contrast, chemokine expression in spleens from mice infected with the plant strain increased over time, whereas chemokine levels in spleens from mice infected with the clinical isolates remained low or near baseline. Protein quantification by ELISA at 5 dpi confirmed these transcriptional trends and additionally revealed increased IFN-γ production in response to the clinical isolates (Fig. S2a).

A comparable phenotype was evident in the kidney at 5 dpi (Fig. 2d). While cytokine expression in kidneys infected with the clinical isolates remained elevated, with the exception of *IL-6*, which was no longer increased, chemokine expression was markedly reduced compared with mice infected with the plant strain. Consistent with the 2 dpi data, *TNF* expression was not significantly induced in the kidney at this later time point. ELISA measurements at 5 dpi corroborated the qPCR findings, showing similar isolate-specific patterns at the protein level (Fig. S2b).

Anti-inflammatory cytokines exhibited a distinct, isolate-dependent pattern that paralleled the cytokine–chemokine uncoupling observed in mice infected with the clinical strains. At early time points, *IL-10* and *TGF-β* transcripts showed a modest increase in response to the clinical isolates compared to the plant strain (Fig. 2a,b). By 5 dpi, *IL-10* and *TGF-β* expression increased across all groups; however, their transcript levels were significantly higher in the spleens and kidneys of mice infected with the clinical isolates compared to those infected with the plant strain.

IL-10 and TGF-β are potent immunoregulatory cytokines known to suppress myeloid cell activation and to dampen chemokine production and responsiveness[34–36], their enrichment in

mice infected with the clinical isolates, therefore, provides a biologically plausible framework to explain the coexistence of sustained pro-inflammatory cytokine production with progressively impaired chemokine expression and leukocyte recruitment.

Together, these data demonstrate that clinical *F. oxysporum* isolates drive a sustained and amplified cytokine response within infected organs, while failing to induce or maintain robust chemokine expression at later stages of infection. In contrast, the plant strain elicits a more balanced inflammatory profile characterized by comparatively restrained cytokine induction and a progressive chemokine response over time. This divergence in inflammatory programming parallels the distinct fungal burden kinetics observed between isolates, supporting the notion that, in this model, sustained chemokine responses and effective inflammatory cell recruitment, rather than elevated cytokine production alone, are required for immune-mediated containment and restriction of fungal invasion in vivo.

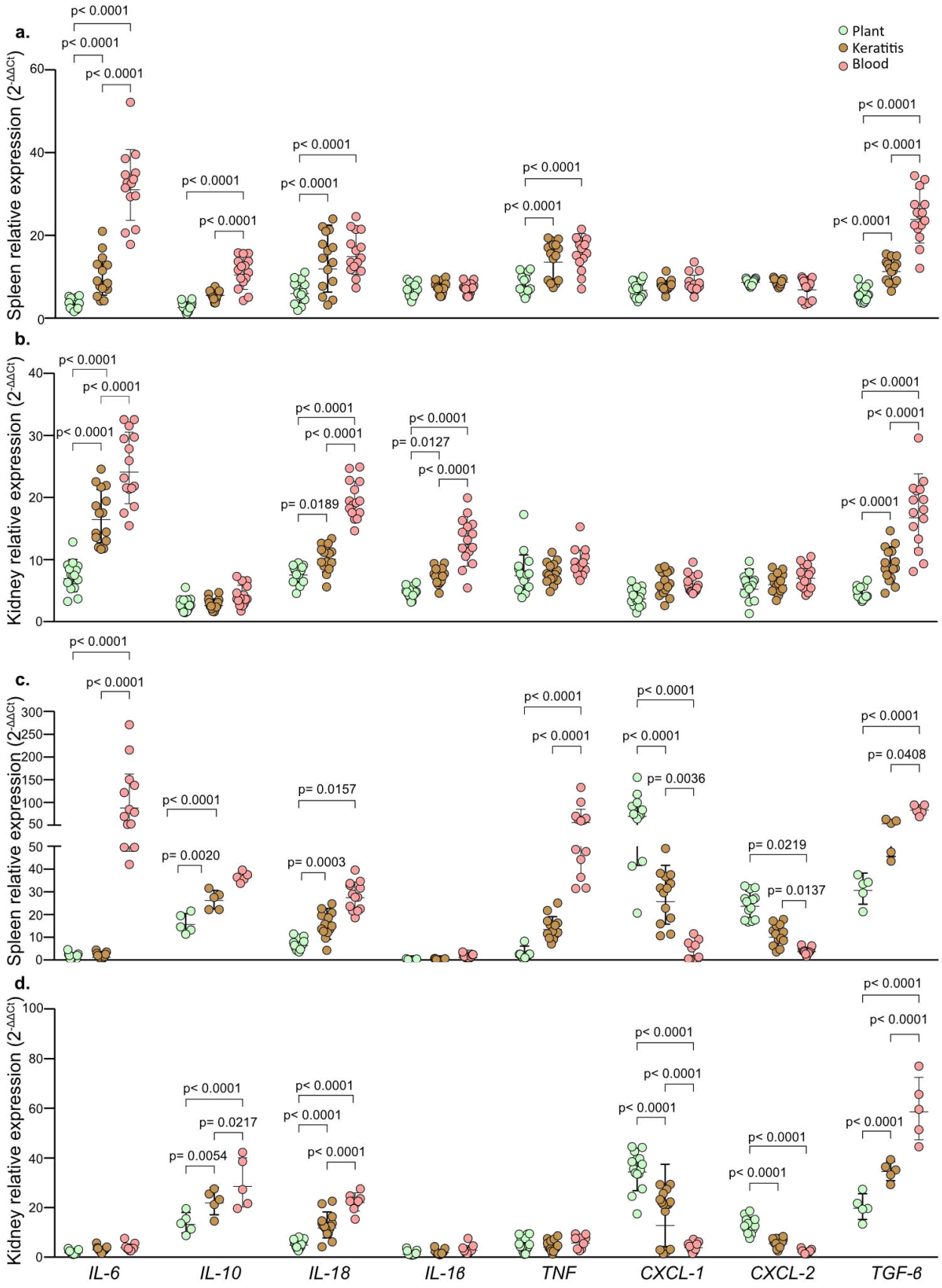

a.
b.
c.
d.
Plant
Keratitis
Blood
Spleen relative expression (2-ΔΔCt)
Kidney relative expression (2-ΔΔCt)
p< 0.0001
p= 0.0127
p= 0.0189
p= 0.0157
p= 0.0020
p= 0.0003
p= 0.0036
p= 0.0219
p= 0.0137
p= 0.0408
p= 0.0054
p= 0.0217
IL-6
IL-10
IL-18
IL-1ß
TNF
CXCL-1
CXCL-2
TGF-ß

Figure 2. Distinct cytokine and chemokine expression profiles elicited by clinical and plant *F. oxysporum* strains. (a–d) RT–qPCR analysis of cytokine and chemokine transcript levels in spleen and kidney from cyclophosphamide-immunosuppressed mice intravenously infected with 1×10^6 microconidia of the plant-derived isolate Fol4287 or the clinical isolates MRL8996 and NRRL32931. Relative mRNA abundance ($2^{-\Delta\Delta ct}$) for *IL-6*, *IL-10*, *IL-18*, *IL-1β*, *TNF*, *CXCL1*, *CXCL2*, and *TGF-β* is shown at 2 dpi in spleen (a) and kidney (b), and at 5 dpi in spleen (c) and kidney (d). Transcript levels were normalized to *ACTβ* and expressed relative to uninfected animals. Each dot represents an individual mouse; bars indicate mean ± s.d. Statistical analysis: (a-d) one-way ANOVA with Tukey's multiple comparisons test; exact *P* values are shown.

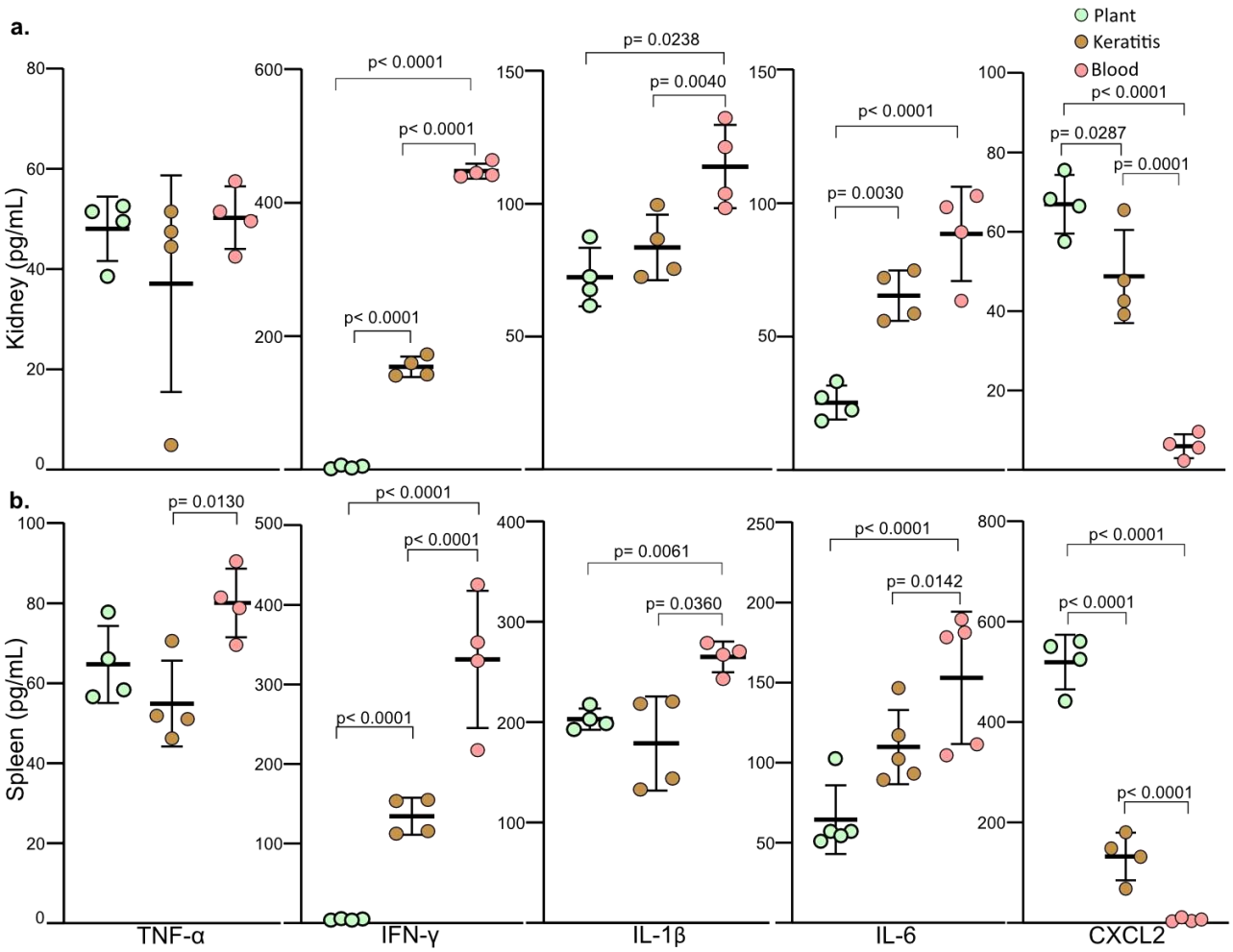


Figure S2: Protein-level cytokine and chemokine responses differ between plant and clinical *F. oxysporum* strains. (a,b) Cytokine and chemokine concentrations measured by ELISA in homogenates of kidney (a) and spleen (b) from cyclophosphamide-immunosuppressed mice intravenously infected with the plant-derived isolate Fol4287 or the clinical isolates MRL8996 and NRRL32931 at 5 dpi. Protein levels of TNF-α, IFN-γ, IL-1β, IL-6, and CXCL2 are shown as pg mL^{-1}. Each dot represents an individual mouse (biologically independent sample); bars indicate mean ± s.d. Statistical analysis: (a-b) one-way ANOVA with Tukey's multiple comparisons test; exact *P* values are shown.

F. oxysporum supernatants from clinical isolates induce caspase-1-dependent pyroptosis in human macrophages

To identify fungal traits that might contribute to the enhanced virulence of clinically derived *F. oxysporum* isolates, we first compared the ability of different strains to induce cytotoxicity in primary human macrophages. Macrophages were exposed to distinct fungal morphotypes, including resting conidia, swollen conidia, and hyphae, derived from each strain. Across all morphotypes tested, the clinical strains (keratitis and blood) induced significantly greater macrophage cytotoxicity than the plant strain, as measured by lactate dehydrogenase (LDH) release (Fig. 3a). We next asked whether this enhanced cytotoxic activity required direct fungal–host contact or could be mediated by secreted factors. To address this, macrophages were exposed to cell-free culture supernatants collected from each strain. Exposure to supernatants alone was sufficient to induce robust macrophage cell death, indicating that *F. oxysporum* secretes soluble factor(s) capable of damaging host cells independently of direct fungal contact (Fig. 3a). Notably, supernatants derived from the clinical strains elicited significantly greater cytotoxicity than those from the plant strain, indicating that the enhanced macrophage damage associated with clinical isolates is largely mediated by secreted fungal products.

Having established that secreted fungal products drive cytotoxicity, we next examined whether these supernatants also recapitulate the inflammatory programs observed in vivo. Exposure of macrophages to *F. oxysporum* culture supernatants induced a rapid transcriptional response characterized by induction of inflammatory mediators, including both cytokines and chemokines

(Fig. 3b,c). Supernatants derived from the clinical strains elicited significantly stronger expression of pro-inflammatory cytokines (*IL-1β*, *IL-18*, *IL-6*, and *TNF*) than those from the plant strain, but were associated with a comparatively attenuated chemokine response, with reduced induction of *CXCL1* and *CXCL2*. This pattern closely mirrors the cytokine–chemokine signatures observed in infected murine tissues, indicating that fungal secreted products play an important role in shaping the strain-specific inflammatory phenotype.

Among the induced mediators, *IL-1β* and *IL-18* were of particular interest, as both encode hallmark cytokines of inflammasome-driven responses and require caspase-1–dependent processing for maturation[36]. Notably, caspase-1 activation also cleaves gasdermin D (GSDMD), unleashing its pore-forming N-terminal fragment that executes pyroptotic cell death[37,38]. Thus, the preferential induction of *IL-1β* and *IL-18* by clinical isolate supernatants, together with the observed cytotoxicity, suggested engagement of an inflammasome-linked, GSDMD-mediated cell death pathway. To test this possibility, caspase-1 activation in macrophages exposed to fungal supernatants was assessed, and the supernatants from the clinical isolates induced robust caspase-1 cleavage, whereas those from the plant strain elicited markedly weaker activation (Fig. 3d; Fig. S3a–c).

We next asked whether the inflammatory and cytotoxic responses elicited by *F. oxysporum* supernatants were functionally dependent on caspase-1 activity. Pharmacological inhibition of caspase-1 prior to stimulation markedly attenuated the induction of pro-inflammatory cytokine transcripts, including *IL-1β*, *IL-18*, *IL-6*, and *TNF*, in response to exposure to clinical isolates (Fig. S3d) or their supernatants (Fig. 3e), indicating that caspase-1 activity is required for their immunomodulatory effect. In contrast, *CXCL1* and *CXCL2* were not induced by clinical isolate supernatants, regardless of caspase-1 inhibition, whereas chemokine induction by the plant strain was caspase-1-dependent and was suppressed by inhibitor treatment.

Finally, we examined whether caspase-1 activation culminates in execution of pyroptotic cell death. Immunoblot analysis revealed prominent cleavage of gasdermin D (GSDMD), generating the characteristic N-terminal pore-forming fragment in macrophages exposed to clinical isolates (Fig. S3e) or their supernatants (Fig. 3f). GSDMD cleavage was substantially reduced following caspase-1 inhibition and correlated with preservation of membrane integrity and reduced LDH

release. Together, these findings establish that secreted product(s) from clinically derived *F. oxysporum* isolates activate a canonical inflammasome–caspase-1–GSDMD axis, driving pyroptotic cell death and shaping the inflammatory response in human macrophages.

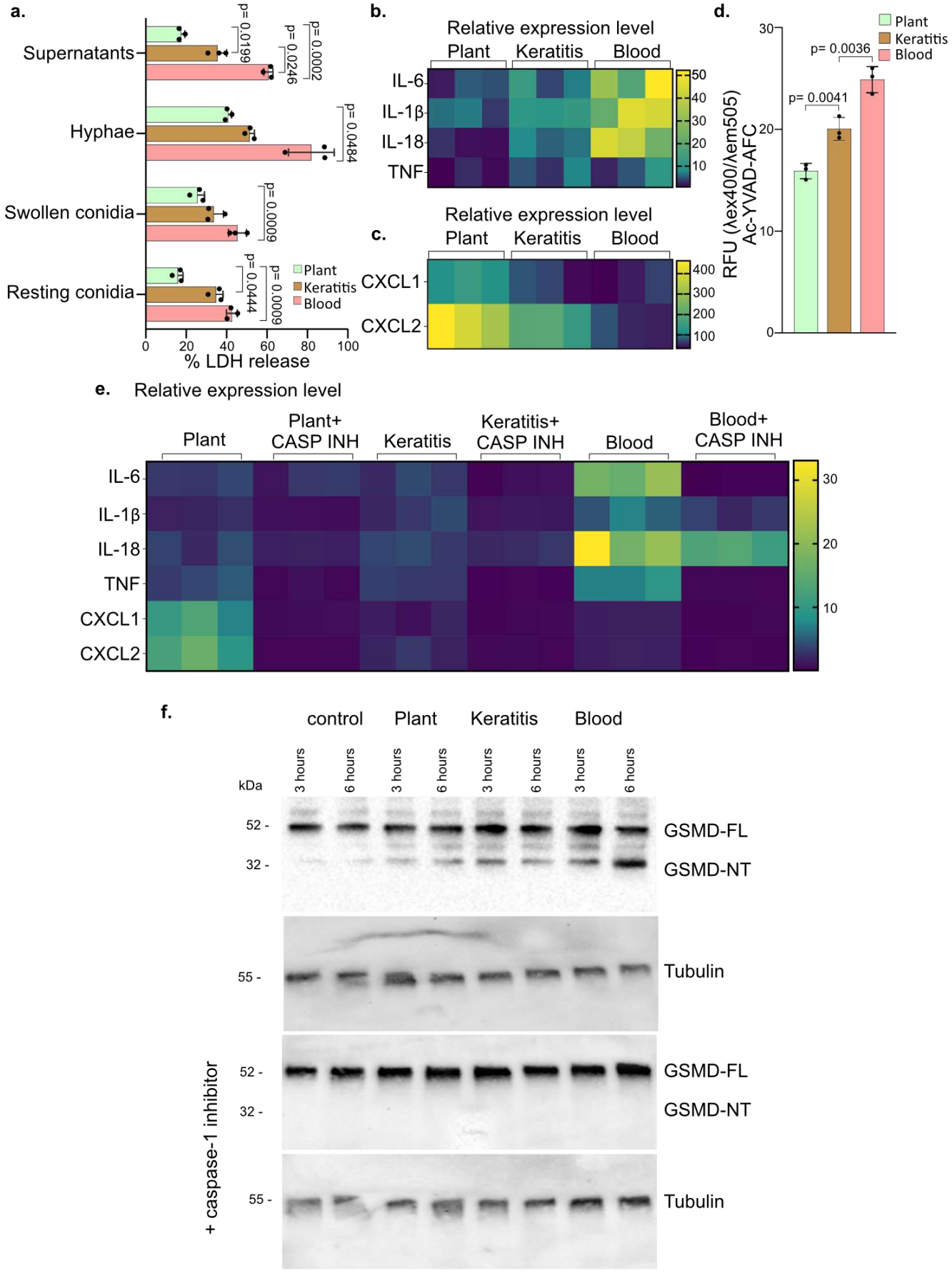
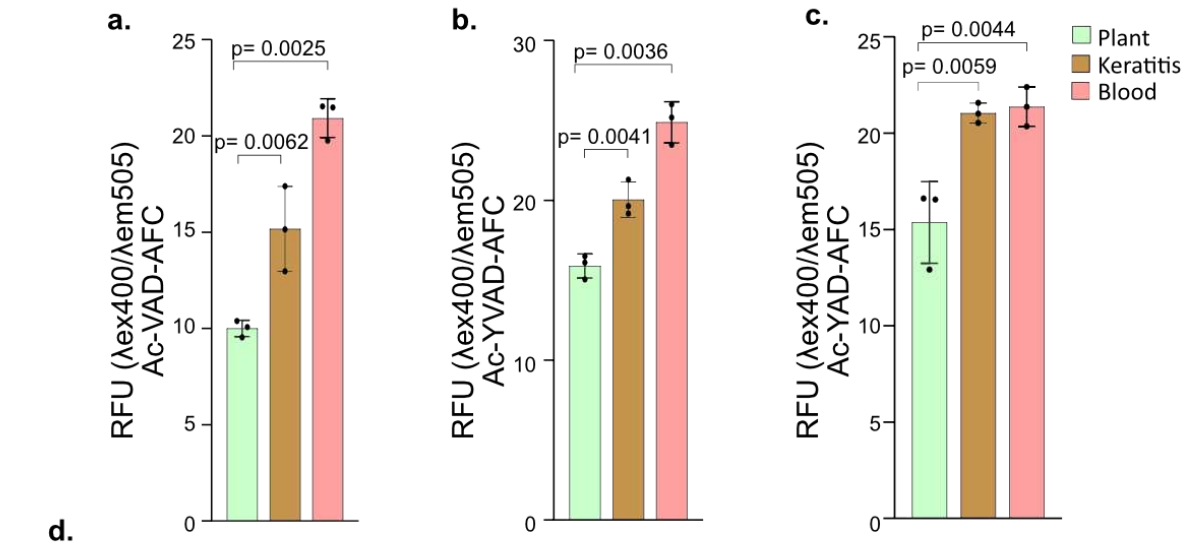
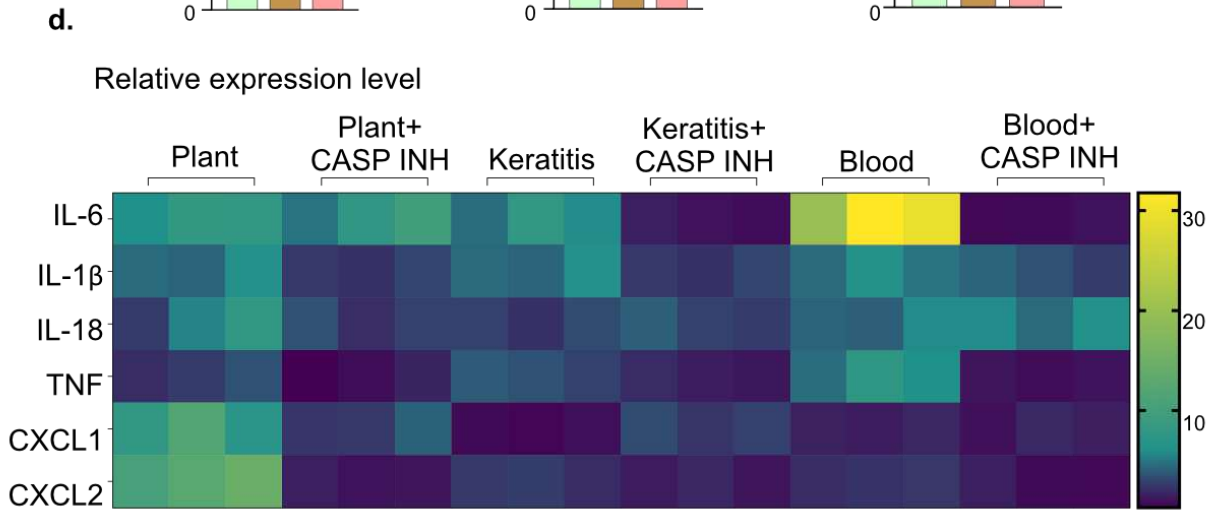

a.
Supernatants
Hyphae
Swollen conidia
Resting conidia
p= 0.0199
p= 0.0246
p= 0.0002
p= 0.0484
p= 0.0009
p= 0.0444
p= 0.0009
Plant
Keratitis
Blood
0
20
40
60
80
100
% LDH release
b.
Relative expression level
Plant
Keratitis
Blood
IL-6
IL-1β
IL-18
TNF
50
40
30
20
10
c.
Relative expression level
Plant
Keratitis
Blood
CXCL1
CXCL2
400
300
200
100
d.
Plant
Keratitis
Blood
p= 0.0036
p= 0.0041
RFU (λex400/λem505)
Ac-YVAD-AFC
30
20
10
0
e.
Relative expression level
Plant
Plant+ CASP INH
Keratitis
Keratitis+ CASP INH
Blood
Blood+ CASP INH
IL-6
IL-1β
IL-18
TNF
CXCL1
CXCL2
30
20
10
f.
control
Plant
Keratitis
Blood
3 hours
6 hours
kDa
52 -
32 -
GSMD-FL
GSMD-NT
55 -
Tubulin
+ caspase-1 inhibitor
52 -
32 -
GSMD-FL
GSMD-NT
55 -
Tubulin

Figure 3: Secreted factors from clinical *F. oxysporum* isolates drive caspase-1-dependent inflammatory programming and pyroptotic cell death in human macrophages. (a) LDH release from human PBMC-derived macrophages following 6 h exposure to resting conidia, swollen conidia, hyphae, or cell-free culture supernatants (collected after 16 h growth in DMEM) from the plant strain (Fol4287), the keratitis strain MRL8996, and the blood strain NRRL32931. LDH release is expressed as a percentage of maximal lysis induced by lysis buffer (b,c). Heat maps of RT–qPCR analysis of cytokine transcripts (*IL-6*, *IL-1β*, *IL-18,* and *TNF*; b) and chemokine transcripts (*CXCL1* and *CXCL2*; c) in PBMC-derived macrophages after 6 h stimulation with strain-matched culture supernatants. Values represent relative mRNA abundance ($2^{-\Delta\Delta Ct}$) normalized to *GAPDH* and calibrated to unstimulated controls. Columns represent independent replicates; color scale indicates relative induction. (d) Caspase-1 activity in macrophages following supernatant stimulation, quantified using a fluorogenic VAD substrate and reported as relative fluorescence intensity (RFI). (e) RT–qPCR analysis of cytokine and chemokine transcripts as in (b,c) following macrophage stimulation with culture supernatants in the absence or presence of caspase-1 inhibition (pre-treatment prior to stimulation). (f) Western blot analysis of gasdermin D (GSDMD) processing in PBMC-derived macrophages stimulated with the indicated supernatants for 3 h or 6 h, showing full-length GSDMD (GSDMD-FL) and the cleaved N-terminal fragment (GSDMD-NT). Tubulin serves as a loading control. Where indicated, macrophages were pre-treated with a caspase-1 inhibitor prior to stimulation. In all panels, each dot or column represents an independent biological replicate; bars indicate mean ± s.d. Exact *P* values are shown where applicable. Statistical analysis: (a,d) one-way ANOVA with Tukey's multiple comparisons test.


a.
b.
c.
RFU (λex400/λem505) Ac-VAD-AFC
RFU (λex400/λem505) Ac-YVAD-AFC
RFU (λex400/λem505) Ac-YAD-AFC
p= 0.0025
p= 0.0062
p= 0.0036
p= 0.0041
p= 0.0044
p= 0.0059
Plant
Keratitis
Blood


d.
Relative expression level
Plant
Plant+ CASP INH
Keratitis
Keratitis+ CASP INH
Blood
Blood+ CASP INH
IL-6
IL-1β
IL-18
TNF
CXCL1
CXCL2

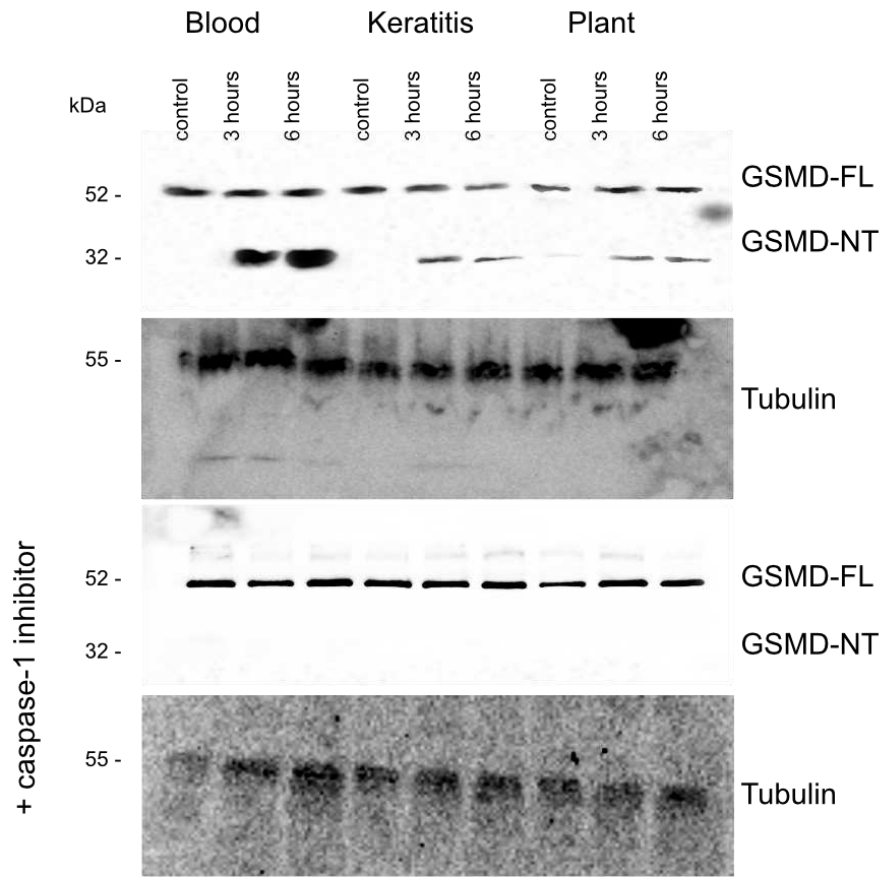

e.
Blood
Keratitis
Plant
kDa
control
3 hours
6 hours
GSMD-FL
GSMD-NT
Tubulin
+ caspase-1 inhibitor

Figure S3: Caspase-1 activation and gasdermin D processing in human macrophages stimulated with *F. oxysporum*. (a) Caspase-1 activity in primary human PBMC-derived macrophages following stimulation with swollen conidia of the plant strain Fol4287, the keratitis strain MRL8996, or the blood strain NRRL32931. Caspase-1 (a) and Caspase-1/4 (c,d) activity was quantified by cleavage of the fluorogenic substrate Ac-VAD-AFC (a) or Ac-YVAD-AFC (c,d). Dots indicate individual replicates and bars show mean ± s.d. Exact *P* values for indicated comparisons are shown. (d) Heat map of RT–qPCR quantification of cytokine transcripts (*IL-6*, *IL-1β*, *IL-18* and *TNF*) and chemokine transcripts (*CXCL1* and *CXCL2*) in PBMC-derived macrophages after 6 h stimulation with *F. oxysporum* swollen conidia in the absence or presence of caspase-1 inhibition (pre-treatment prior to stimulation). Values represent relative mRNA abundance ($2^{-\Delta\Delta Ct}$) normalized to a *GAPDH* and calibrated to unstimulated controls. Columns represent independent replicates; color scale indicates relative induction. (e) Western blot analysis of gasdermin D (GSDMD) processing in PBMC-derived macrophages stimulated with the indicated swollen conidia from the isolates for 3 h or 6 h following pre-treatment with a caspase-1 inhibitor. Full-length GSDMD (GSDMD-FL) and the cleaved N-terminal fragment (GSDMD-NT) are shown. Tubulin serves as a loading control. Where indicated, macrophages were pre-treated with a caspase-1 inhibitor prior to stimulation. In all panels, each dot or column represents an independent biological replicate; bars indicate mean ± s.d. Exact *P* values are shown where applicable. Statistical analysis: (a-c) one-way ANOVA with Tukey's multiple comparisons test.

Clinical *F. oxysporum* isolates exhibit altered ergosterol homeostasis and increased resistance to sterol-targeting antifungal agents

We next sought to identify the fungal factor responsible for the secreted cytotoxic and immunomodulatory activity of the clinical isolates. Pyroptotic cell death is commonly initiated by microbial products that engage inflammasome signaling, and sterols such as cholesterol are established inducers of inflammasome activation in myeloid cells[39]. Notably, the fungal sterol ergosterol has also been implicated in macrophage cell death during *Candida* infection[40,41], suggesting that altered sterol biology could contribute to the observed phenotype. Therefore, we

hypothesized that clinical *F. oxysporum* isolates differ from the plant strain in ergosterol homeostasis, with consequences for both antifungal susceptibility and host immune activation. As an initial functional assessment of sterol biology, the susceptibility of the isolates to antifungal drugs that target ergosterol synthesis or function were compared. The two clinical isolates exhibited reduced susceptibility to the azole antifungals fluconazole and voriconazole, which inhibit ergosterol biosynthesis, as well as to amphotericin B, which binds ergosterol directly (Fig. 4a; Fig. S4a). Across all conditions, the clinical strains maintained greater radial growth than the plant strain, with the bloodstream isolate showing the most pronounced phenotype, including sustained growth at fluconazole concentrations that fully suppressed the plant strain. These data indicate an isolate-specific difference in responses to ergosterol-targeting antifungals.

To determine whether altered drug accumulation might contribute to this phenotype, we monitored the uptake and subcellular distribution of a fluorescent fluconazole analog in live hyphae[42]. The plant strain displayed strong intracellular fluorescence with a perinuclear distribution consistent with accumulation near the endoplasmic reticulum (ER), the site of the azole target lanosterol 14α-demethylase (CYP51/ERG11)[43]. In contrast, both clinical isolates exhibited significantly reduced intracellular fluorescence, with the weakest signal observed in the blood strain (Fig. 4b). The altered signal intensity and distribution suggest reduced intracellular availability of fluconazole in the clinical strains, which could reflect decreased uptake, enhanced efflux, altered intracellular trafficking, or a combination of these mechanisms. While our data do not distinguish among these possibilities, they indicate that reduced drug accumulation accompanies azole resistance in the clinical isolates.

We next directly assessed sterol output by quantifying ergosterol in culture supernatants and at the cell surface using GC–MS and flow cytometry (Fig. 4c; Fig. S4e). Both clinical isolates released significantly higher levels of ergosterol than the plant strain, with the blood strain exhibiting a multi-fold increase. Elevated extracellular ergosterol could arise from increased biosynthesis, or altered membrane turnover, sterol trafficking and export. Nonetheless, the consistent increase in extracellular ergosterol observed in both clinical isolates prompted us to investigate whether isolate-specific differences in sterol pathway regulation might underlie this phenotype.

To investigate the molecular basis underlying these differences, we examined expression of ergosterol biosynthesis and regulatory genes across fungal developmental stages, including resting conidia, swollen conidia, hyphae, and swollen conidia exposed to macrophage stress (+MACS) (Fig. 4d,e; Fig. S4b-d). Baseline transcriptional differences were minimal in conidia (resting and swollen) but became more apparent during hyphal growth, with several sterol-pathway genes expressed at higher levels in the clinical isolates. Macrophage exposure (+MACS) further amplified this divergence, eliciting a stronger induction of sterol-pathway genes in the clinical strains relative to the plant strain. In particular, expression of *ERG11-1* and *ERG11-3*, two out of three genes encoding 14-α sterol demethylase-like enzymes that serve as targets of azole antifungals, increased modestly in the plant strain, but rose more substantially in the blood strain under +MACS conditions (~5–6-fold for *ERG11-1* and ~25-fold for *ERG11-3*) (Fig. 4d; Fig. S4b). Expression of the sterol-responsive transcription factor *UPC2* also increased substantially in the clinical isolates during macrophage stress, whereas induction in the plant strain was comparatively attenuated (Fig. 4e), consistent with isolate-specific regulation of sterol homeostasis rather than uniform pathway activation. Additional sterol-pathway genes also displayed isolate-specific differences during hyphal growth, including *ERG1* and *ERG2*, both of which were more highly expressed in the clinical isolates than in the plant strain (Fig. S4c, d).

Broader transcriptional profiling by RNA-seq revealed coherent, strain-specific patterns across the ergosterol network (Fig. 4f; Fig. S4f–h). Principal component analysis of ergosterol-related genes demonstrated clear segregation of isolates based on sterol pathway expression profiles, underscoring distinct regulatory states. Among the azole targets, *ERG11-3* (*CYP51A*) was elevated in both clinical isolates, whereas *ERG11-2* (*CYP51B*) was selectively increased in the blood strain. Additional sterol-pathway components, including genes encoding late-stage enzymes such as *ERG25* and downstream processing genes such as *ERG2*, displayed isolate-specific increases. Notably, *CYB5* encoding the redox partner was preferentially upregulated in the blood strain. Together, these data indicate differential, strain-dependent regulation of sterol metabolism rather than a uniform increase in pathway activity. Notably, transcripts associated with canonical multidrug efflux pumps (*PDR5* and *AUS1/PDR11*) remained low across isolates under these conditions, suggesting that the dominant transcriptional differences reflect altered sterol pathway regulation rather than a generalized efflux response.

Together, these data identify remodeling of ergosterol homeostasis, encompassing altered antifungal susceptibility, reduced intracellular azole accumulation, increased extracellular ergosterol, and isolate-specific transcriptional remodeling of the sterol biosynthetic network, as a distinguishing feature of clinical *F. oxysporum* isolates. The coordinated changes in sterol-pathway gene expression may contribute to these phenotypes, although additional post-transcriptional or trafficking mechanisms cannot be excluded. This fungal-intrinsic phenotype provides a mechanistic foundation for exploring ergosterol as a candidate mediator of the macrophage pyroptosis and immune modulation observed during infection.

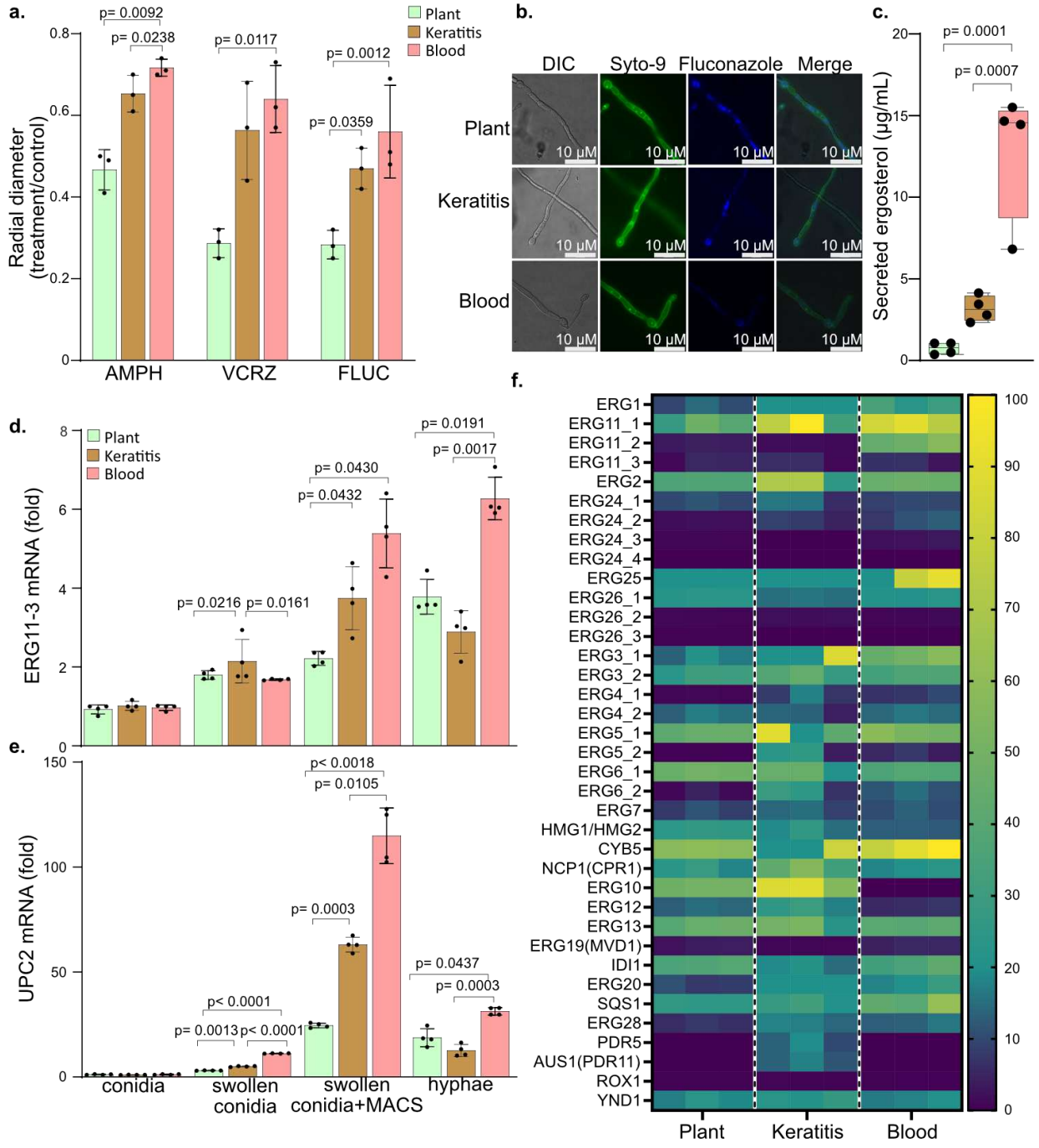


Figure 4: Divergent azole susceptibility in plant and clinical *F. oxysporum* isolates correlates with drug uptake and sterol pathway regulation. (a) Antifungal susceptibility profiles expressed as the ratio of colony radial diameter in drug-treated versus untreated conditions for amphotericin B (AMPH; 0.5 µg mL^{-1}), voriconazole (VCRZ; 2 µg mL^{-1}), or fluconazole (FLUC; 16 µg mL^{-1}). (b) Representative fluorescence microscopy assessing drug

uptake. Hyphae from the plant (Fol4287), keratitis (MRL8996), and blood (NRRL32931) strains were incubated with a fluorescent fluconazole probe (blue; DAPI channel) and counterstained with SYTO 9 (nuclei). (c) Quantification of ergosterol (μg mL^{-1}) in culture supernatants. (d,e) RT–qPCR analysis of the sterol pathway regulators *CYP51A* (*ERG11-3*) (d) and *UPC2* (e) across fungal morphotypes. Relative transcript abundance in resting conidia, swollen conidia, MACS-challenged swollen conidia, and hyphae is expressed as fold change. (f) Heat map of actin-normalized RNA-seq expression counts for sterol biosynthesis and associated genes across the indicated isolates cultured at pH 7.4. In panels a and c, points represent biologically independent replicates; bars indicate mean ± s.d. (a) or box plots showing median and interquartile range (c); *P* values are indicated. Scale bars, 10 μm. In all panels, each dot or column represents an independent biological replicate; bars indicate mean ± s.d. Exact *P* values are shown where applicable. Statistical analysis: (a,c,d,e) one-way ANOVA with Tukey's multiple comparisons test.

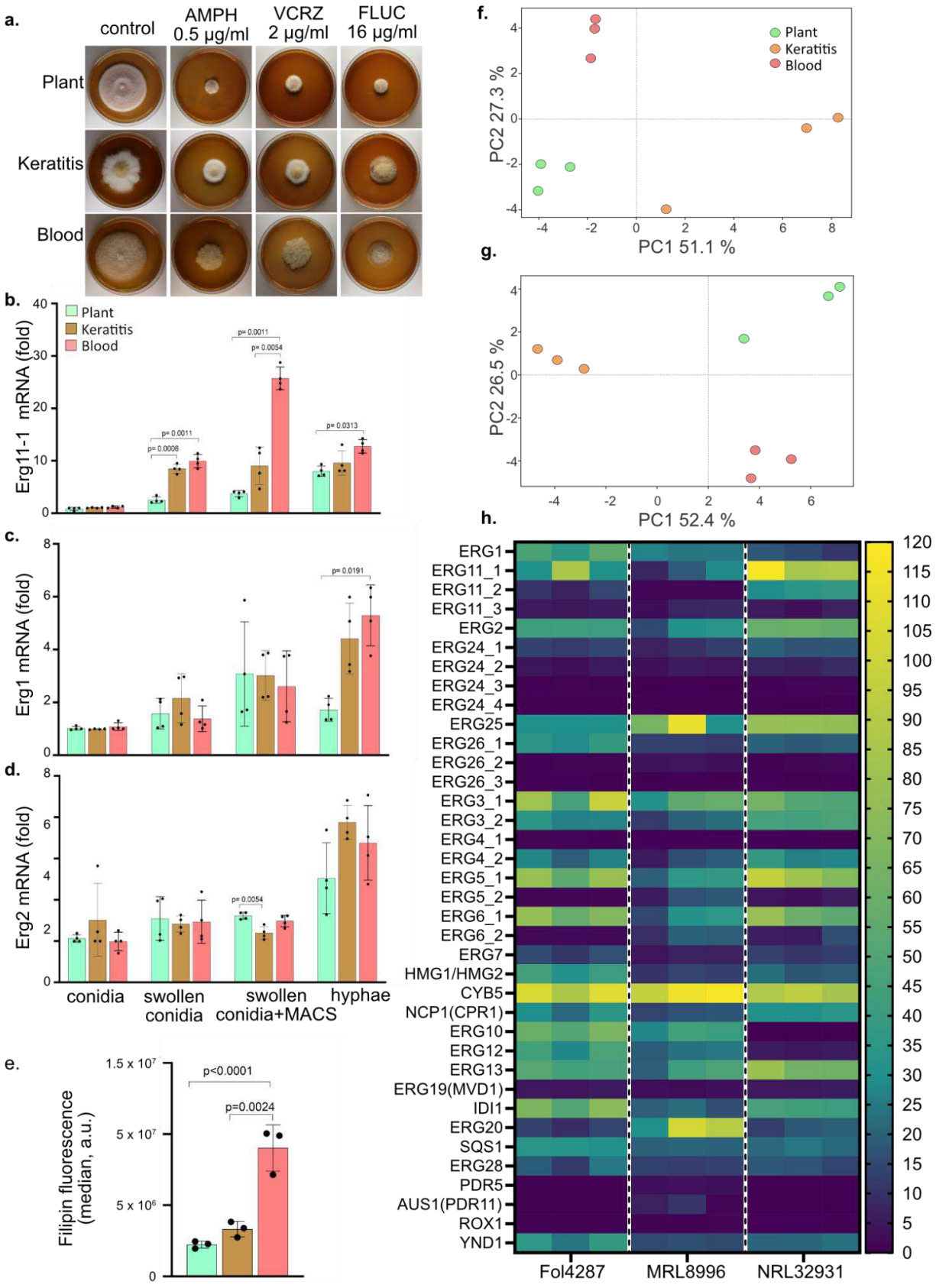

a.
control
AMPH 0.5 µg/ml
VCRZ 2 µg/ml
FLUC 16 µg/ml
Plant
Keratitis
Blood
b.
Plant
Keratitis
Blood
Erg11-1 mRNA (fold)
p= 0.0006
p= 0.0011
p= 0.0011
p= 0.0054
p= 0.0313
c.
Erg1 mRNA (fold)
p= 0.0191
d.
Erg2 mRNA (fold)
p= 0.0054
conidia
swollen conidia
swollen conidia+MACS
hyphae
e.
Filipin fluorescence (median, a.u.)
p<0.0001
p=0.0024
f.
Plant
Keratitis
Blood
PC2 27.3 %
PC1 51.1 %
g.
PC2 26.5 %
PC1 52.4 %
h.
ERG1
ERG11_1
ERG11_2
ERG11_3
ERG2
ERG24_1
ERG24_2
ERG24_3
ERG24_4
ERG25
ERG26_1
ERG26_2
ERG26_3
ERG3_1
ERG3_2
ERG4_1
ERG4_2
ERG5_1
ERG5_2
ERG6_1
ERG6_2
ERG7
HMG1/HMG2
CYB5
NCP1(CPR1)
ERG10
ERG12
ERG13
ERG19(MVD1)
IDI1
ERG20
SQS1
ERG28
PDR5
AUS1(PDR11)
ROX1
YND1
Fol4287
MRL8996
NRL32931

Figure S4: Clinical *F. oxysporum* isolates exhibit altered antifungal susceptibility and strain-specific remodeling of the ergosterol program. **(a)** Representative colony growth of the plant (Fol4287), the keratitis (MRL8996), and the blood (NRRL32931) strains on agar in the absence (control) or presence of amphotericin B (AMPH; 0.5 μg mL^{-1}), voriconazole (VCRZ; 2 μg mL^{-1}), or fluconazole (FLUC; 16 μg mL^{-1}). **(b–d)** RT–qPCR quantification of *ERG11-1* (b), *ERG1* (c), and *ERG2* (d) transcripts across indicated developmental states (resting conidia, swollen conidia, MACs-challenged swollen conidia, and hyphae). Expression is normalized to actin and shown as fold change. Bars indicate mean ± s.d.; points denote independent biological replicates (n = 3). Exact *P* values for selected pairwise comparisons are shown. **(e)** Quantification of membrane-associated ergosterol abundance (peak area) under control conditions. Bars indicate mean ± s.d.; points denote independent biological replicates (n = 3). Exact *P* values are shown. **(f,g)** Principal component analysis (PCA) of replicate-level expression profiles for 37 genes involved in ergosterol biosynthesis and homeostasis, selected from total RNA-seq data at pH 7.4 (**f**) and pH 5 (**g**). Each point represents an independent replicate (n = 3 per strain); the variance explained by PC1 and PC2 is indicated on the axes. **(h)** Heatmap of actin-normalized (scaled) expression values for ergosterol biosynthesis and sterol homeostasis genes across strains at pH 5. Columns represent biological replicates (n = 3 per strain); dashed lines demarcate strain groupings. In all panels, each dot or column represents an independent biological replicate; bars indicate mean ± s.d. Exact *P* values are shown where applicable. Statistical analysis: (b-e) one-way ANOVA with Tukey's multiple comparisons test.

Ergosterol directly induces macrophage pyroptosis and dose-dependent immune modulation

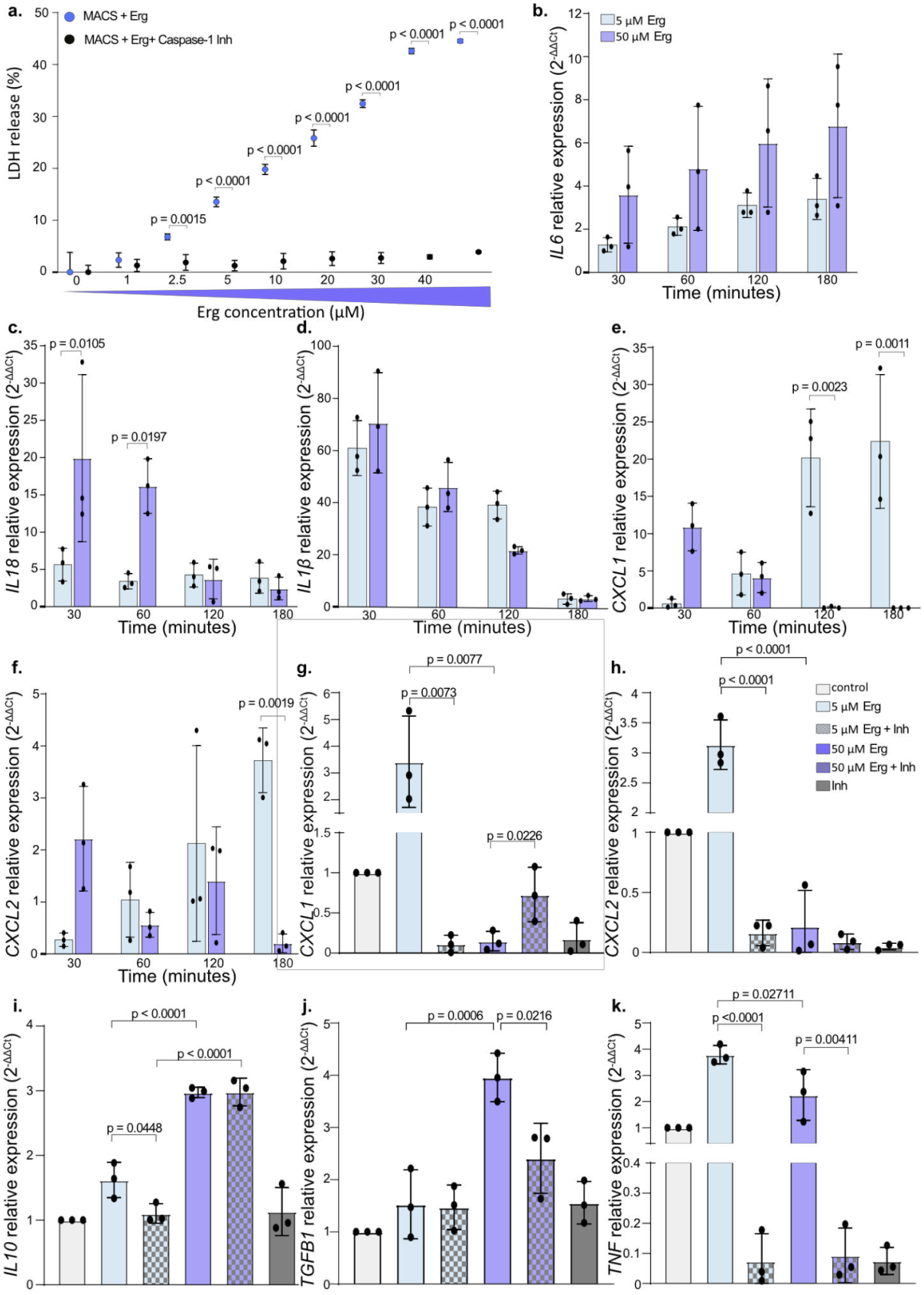
To determine whether ergosterol itself is sufficient to drive the macrophage phenotypes observed in response to clinical isolates, primary human PBMC-derived macrophages were exposed to increasing concentrations of purified ergosterol spanning the range detected in fungal culture supernatants (Fig. 4c). Cytotoxicity was quantified by LDH release. Ergosterol induced macrophage lytic death in a dose-dependent manner (Fig. 5a). At higher concentrations,

cytotoxicity was pronounced and reproducible across independent experiments. Notably, pre-treatment with a broad caspase inhibitor completely abrogated ergosterol-induced LDH release, restoring cell viability to baseline levels. These data demonstrate that extracellular ergosterol is sufficient to induce caspase-dependent macrophage death consistent with pyroptosis.

We next examined transcriptional responses to low (5 μM) and high (50 μM) ergosterol concentrations, corresponding to levels detected in supernatants derived from the plant and the clinical strains, respectively. Both doses induced expression of inflammasome- and pyroptosis-associated cytokines, including *IL-6*, *IL-1β*, and *IL-18*. While induction of *IL-6* and *IL-18* increased with ergosterol concentration, *IL-1β* expression was robustly induced at both doses (Fig. 5b-d). These findings support a model in which ergosterol directly promotes inflammatory signaling linked to pyroptotic activation. In contrast, chemokine responses exhibited a dose-dependent divergence. Low ergosterol induced robust expression of *CXCL1* and *CXCL2*, whereas high ergosterol markedly suppressed their expression (Fig. 5e-f). This biphasic regulation mirrors the in vivo and ex vivo observations that high-ergosterol–producing clinical isolates attenuate chemokine induction. High ergosterol also increased expression of the anti-inflammatory cytokines *IL-10* and *TGF-β* (Fig. 5i-j), consistent with a potential role for ergosterol in promoting an immunomodulatory transcriptional program that restrains chemokine output.

To assess the contribution of NF-κB signaling, macrophages were treated with the IκB kinase (IKK) inhibitor BAY 11-7082 prior to ergosterol stimulation. Inhibition of NF-κB signaling effectively suppressed *TNF* induction (Fig. 5k), confirming inhibitor activity. Under low-ergosterol conditions, BAY 11-7082 significantly reduced *CXCL1* and *CXCL2* expression, indicating that chemokine induction at low sterol concentrations is NF-κB dependent (Fig. 5g-h). Under high-ergosterol conditions, BAY 11-7082 partially restored *CXCL1* expression but did not rescue *CXCL2* levels, which remained suppressed (Fig. 5g-h). These findings suggest that high-ergosterol–mediated repression of *CXCL1* is at least partly NF-κB dependent, whereas *CXCL2* suppression occurs through an NF-κB–independent mechanism. Notably, *IL-10* induction was unaffected by NF-κB inhibition, while *TGF-β* expression was reduced in the presence of BAY 11-7082, indicating differential pathway requirements for these anti-inflammatory mediators. Together, these findings demonstrate that extracellular ergosterol is sufficient to induce caspase-

dependent macrophage pyroptosis and to impose a concentration-dependent reprogramming of inflammatory outputs. High ergosterol levels promote inflammasome-associated cytokine expression (including *IL-6* and *IL-18*) while simultaneously inducing the anti-inflammatory mediators *IL-10* and *TGF-β*, in parallel with suppression of the neutrophil-attracting chemokines *CXCL1* and *CXCL2*. These data indicate that ergosterol does not globally inhibit macrophage activation but instead selectively redirects inflammatory signaling in a concentration-dependent manner. The differential sensitivity of these responses to NF-κB inhibition further suggests that ergosterol engages both NF-κB–dependent and –independent regulatory pathways to shape macrophage activation.


a.
MACS + Erg
MACS + Erg+ Caspase-1 Inh
LDH release (%)
p = 0.0015
p < 0.0001
Erg concentration (μM)
b.
5 μM Erg
50 μM Erg
IL6 relative expression (2-ΔΔCt)
Time (minutes)
c.
IL18 relative expression (2-ΔΔCt)
p = 0.0105
p = 0.0197
d.
IL1β relative expression (2-ΔΔCt)
e.
CXCL1 relative expression (2-ΔΔCt)
p = 0.0023
p = 0.0011
f.
CXCL2 relative expression (2-ΔΔCt)
p = 0.0019
g.
CXCL1 relative expression (2-ΔΔCt)
p = 0.0077
p = 0.0073
p = 0.0226
h.
CXCL2 relative expression (2-ΔΔCt)
p < 0.0001
control
5 μM Erg
5 μM Erg + Inh
50 μM Erg
50 μM Erg + Inh
Inh
i.
IL10 relative expression (2-ΔΔCt)
p = 0.0448
j.
TGFB1 relative expression (2-ΔΔCt)
p = 0.0006
p = 0.0216
k.
TNF relative expression (2-ΔΔCt)
p = 0.02711
p <0.0001
p = 0.00411

609

Figure 5: Ergosterol-rich secretomes drive macrophage inflammatory activation and cytotoxicity. (a) LDH release from PBMC-derived macrophages exposed to increasing concentrations of purified ergosterol, in the presence or absence of a caspase-1 inhibitor. (b–f) RT–qPCR analysis of inflammatory mediator expression in PBMC-derived macrophages stimulated with low or high concentrations of ergosterol, showing relative mRNA abundance ($2^{-\Delta\Delta Ct}$) of *IL-6* (b), *IL-18* (c), *IL-1β* (d), *CXCL1* (e), and *CXCL2* (f). (g–k) RT–qPCR analysis of ergosterol-responsive genes in macrophages treated with ergosterol in the presence or absence of the NF-κB inhibitor BAY 11-7082, showing relative mRNA abundance ($2^{-\Delta\Delta Ct}$) of *CXCL1* (g), *CXCL2* (h), *IL-10* (i), *TGF-β* (j), and *TNF* (k). For inhibitor experiments, macrophages were preincubated with BAY 11-7082 before stimulation with the indicated ergosterol concentrations for 6 h. RNA was extracted and transcript levels were quantified by RT–qPCR using *GAPDH* as the endogenous control. Data are representative of three independent experiments. Dots indicate individual biological replicates; bars indicate mean ± s.d. In all panels, each dot or column represents an independent biological replicate; bars indicate mean ± s.d. Exact *P* values are shown where applicable. Statistical analysis: (a,d) one-way ANOVA with Tukey's multiple comparisons test.

Ergosterol-associated phenotypes are enriched among clinically derived *F. oxysporum* isolates

To determine whether the ergosterol-associated cytotoxic phenotype observed in the reference strains extends to a broader population, we analyzed an expanded panel of environmentally (soil-derived) and clinically derived *F. oxysporum* isolates. We quantified total extracellular lipids, which include ergosterol and related sterol species, from cell-free culture supernatants (Bligh–Dyer) and related these measurements to macrophage cytotoxicity, assessed by LDH release following supernatant exposure. Across the panel, extracellular lipid abundance positively correlated with macrophage lysis (Fig. 6a). Environmentally derived isolates predominantly clustered within a low-lipid/low-cytotoxicity range, whereas clinically derived isolates were enriched at the higher end of both parameters. Consistent with this trend, individual clinical isolates combined increased lipid release with elevated macrophage cytotoxicity, supporting an association between enhanced extracellular lipid output and host cell damage (Fig. 6a).

Based on these findings, we propose that within the broader diversity of *F. oxysporum*, isolates with intrinsically higher ergosterol production and subsequent release are more likely to elicit macrophage pyroptosis while suppressing chemokine-driven immune cell recruitment, thereby conferring increased pathogenic potential (Fig. 6b). In this model, augmented ergosterol output does not simply amplify inflammation but selectively reprograms host responses toward lytic, immunomodulatory outcomes that may favor fungal persistence and dissemination.

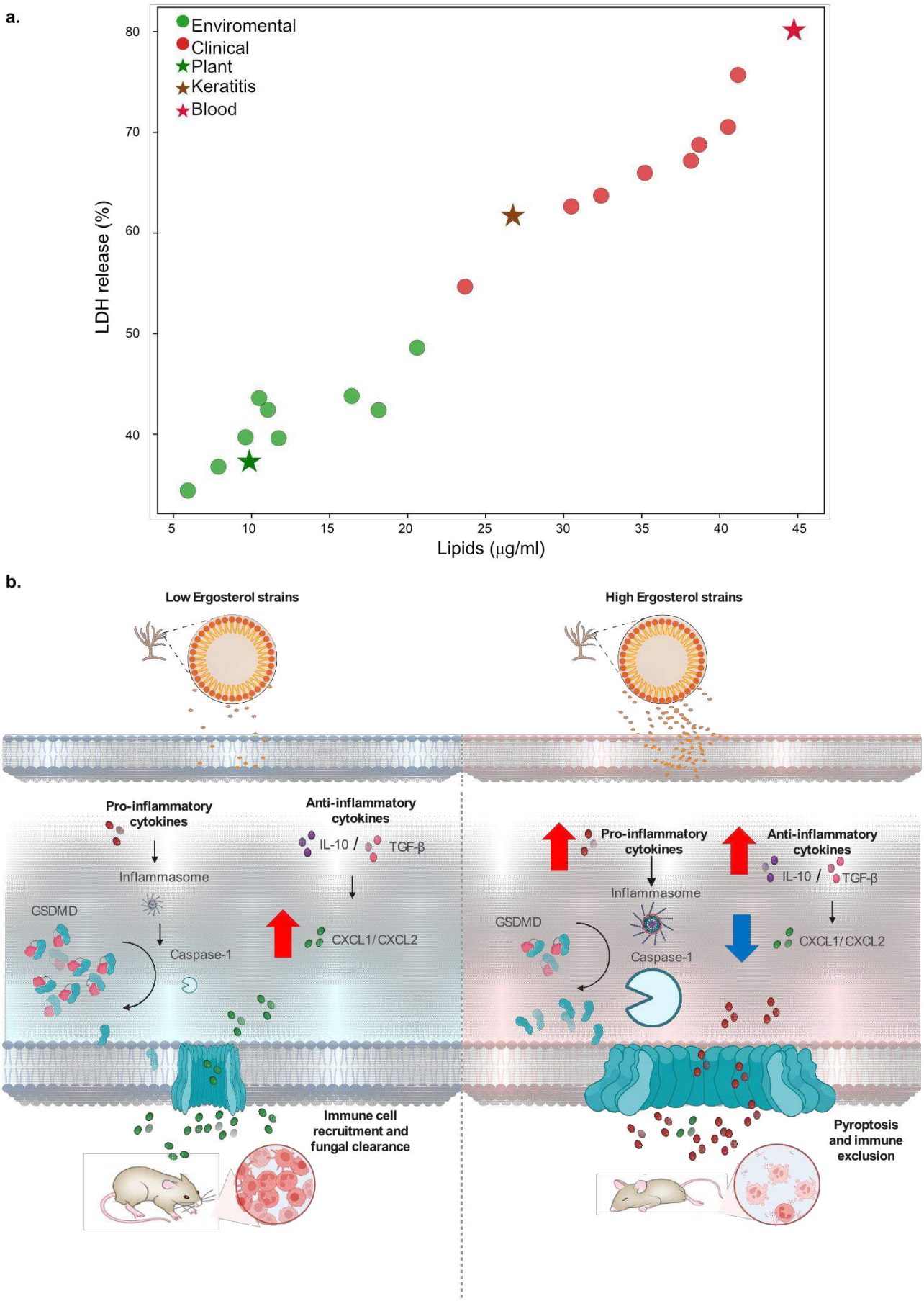

a.
Enviromental
Clinical
Plant
Keratitis
Blood
LDH release (%)
Lipids (μg/ml)
b.
Low Ergosterol strains
High Ergosterol strains
Pro-inflammatory cytokines
Anti-inflammatory cytokines
IL-10 / TGF-β
Inflammasome
GSDMD
Caspase-1
CXCL1/CXCL2
Immune cell recruitment and fungal clearance
Pyroptosis and immune exclusion

Figure 6. Ergosterol abundance predicts macrophage lysis and shapes inflammatory outcomes during *F. oxysporum* infection. (a) Total lipids extracted from culture supernatants of germinated conidia for 16 h (μg mL^{-1}) were plotted against macrophage membrane damage induced by the corresponding supernatants, measured by LDH release (%) in human derived macrophages. Lipids were extracted from fungal supernatants using the Bligh and Dyer method, quantified by final dry weight, and normalized to fungal dry mass. Each symbol represents one isolate. Environmental (soil-derived) isolates are shown as green circles, whereas clinical isolates are shown as red circles. Stars indicate the three strains used throughout the study: the plant isolate (Fol4287), the keratitis isolate (MRL8996), and the blood isolate (NRRL32931). (b) Proposed model of ergosterol-mediated immunomodulation by *F. oxysporum*. Isolates with intrinsically elevated ergosterol output promote macrophage inflammasome activation, leading to caspase-1–dependent gasdermin D (GSDMD) cleavage, and pyroptotic cell lysis. This response is associated with robust expression of *IL-1β, IL-18*, and *IL-6*, together with induction of the anti-inflammatory cytokines *IL-10* and *TGF-β*. These responses may contribute to a functional decoupling between cytokine production and chemokine-mediated immune cell recruitment.

Discussion

The emergence of *F. oxysporum* as a major cause of fungal keratitis and invasive fusariosis challenges the traditional separation between plant pathology and medical mycology. Because clinical and non-clinical isolates originate from diverse environmental niches and share pathogenic capacity across hosts, it remains unclear which traits are enriched in strains that disproportionately cause severe invasive disease in humans. Our data identify remodeling of ergosterol homeostasis as a distinguishing trait of clinically derived isolates and implicate sterol remodeling as a mechanistic link between fungal physiology and pathogenic behavior in mammalian hosts.

Rather than requiring the acquisition of entirely novel virulence determinants, our findings suggest that quantitative remodeling of sterol metabolism shapes host–pathogen interactions and contribute to the enhanced pathogenic potential of clinical isolates. Clinical isolates exhibited increased extracellular ergosterol, altered azole accumulation, reduced azole susceptibility, and strain-specific transcriptional remodeling of sterol pathway genes. Although ergosterol is primarily a membrane lipid, sterols can be released during membrane remodeling or packaged

into extracellular vesicles[44,45], raising the possibility that altered sterol trafficking or export contributes to the elevated extracellular ergosterol levels observed in clinical isolates. Functionally, this sterol-enriched state drove two coordinated immunological outcomes: enhanced macrophage pyroptosis and selective suppression of chemokine-driven cellular recruitment. Together, these effects created a localized failure of innate containment despite robust proinflammatory cytokine induction.

Sterols are increasingly recognized as modulators of innate immune signaling. Cholesterol crystals are well-established activators of inflammasome pathways in myeloid cells[46,47], and fungal sterols such as ergosterol have previously been implicated in macrophage death during *Candida* infection[41,48]. However, whether extracellular ergosterol can directly reprogram macrophage inflammatory responses has remained largely unexplored. Consistent with this possibility, our data indicate that pyroptotic macrophage death alone does not fully explain the immune phenotype. While caspase-1/GSDMD-dependent pyroptosis contributed to early loss of resident phagocytes and amplified IL-1β/IL-18 release, our data indicate that ergosterol also reprograms macrophage inflammatory outputs in a concentration-dependent manner. High extracellular ergosterol induced strong *TNF-α*, *IL-1β*, and *IL-18* expression while simultaneously suppressing *CXCL1* and *CXCL2*. This decoupling of cytokine production from chemokine-mediated neutrophil recruitment cannot be attributed solely to cell lysis; rather, it reflects selective transcriptional reprogramming. A key mechanistic feature of this reprogramming was the induction of *IL-10* and *TGF-β* in response to high ergosterol exposure. These immunoregulatory cytokines are well-established suppressors of chemokine expression and neutrophil recruitment, acting through STAT3 and SMAD-dependent pathways to restrain excessive inflammation[49,50]. We propose that ergosterol induces a bifurcated signaling program: activation of inflammasome and NF-κB pathways driving proinflammatory cytokines, coupled with compensatory induction of *IL-10*/*TGF-β* that selectively dampens chemokine outputs. The net result is a paradoxical inflammatory state characterized by systemic cytokine elevation but impaired cellular recruitment. Similar patterns of cytokine–chemokine uncoupling have been described in bacterial infections and sepsis, where inflammasome activation coexists with defective neutrophil trafficking[51,52]. In this context, ergosterol functions not merely as a membrane sterol but as an immunomodulatory metabolite and bona fide virulence determinant capable of reshaping innate immune circuitry.

The biphasic nature of the effects of ergosterol further supports a threshold model. At concentrations approximating those released by non-clinical isolates, macrophages mounted a controlled inflammatory response with preserved chemokine production. At higher concentrations, comparable to clinical isolate secretomes, ergosterol became immunoregulatory and cytotoxic, promoting pyroptosis and chemokine suppression. Such concentration-dependent immune modulation resembles the behavior of other lipid mediators and damage-associated signals, which transition from homeostatic to pathological functions above defined thresholds. Extracellular ATP released from damaged host cells activates P2X7-dependent NLRP3 signaling when present at high concentrations[32,53], while sterol-derived host danger signals such as cholesterol crystals trigger inflammasome activation above homeostatic thresholds[54]. Likewise, lipid mediators including prostaglandin E_2 exert dose-dependent immunoregulatory effects, suppressing chemokine production and promoting *IL-10*–associated pathways when sustained or elevated[55]. These precedents provide a conceptual framework for understanding how quantitative increases in fungal sterol flux, rather than the mere presence of ergosterol, may distinguish non-clinical from clinical phenotypes. From a pathogenesis perspective, the combined effects of enhanced pyroptosis and reduced neutrophil recruitment create an "immune exclusion" microenvironment. Rapid inflammasome activation eliminates macrophages that would otherwise coordinate chemotaxis, while suppressed *CXCL1*/*CXCL2* expression limits neutrophil influx. The resulting tissue niche contains abundant inflammatory cytokines but insufficient effector cells. In neutropenic hosts, this imbalance is further amplified, as cytokine signals lack their principal cellular responders. Thus, ergosterol-driven immune dysregulation converts protective inflammation into tissue-damaging, non-resolving pathology.

These observations also raise questions about the ecological contexts in which sterol-enriched phenotypes may arise. *F. oxysporum* is fundamentally an environmental fungus that inhabits diverse ecological niches, including soil and plant-associated environments, where populations may encounter a variety of stressors, including azole fungicides used in agricultural[56]. Under conditions in which environmental populations experience sterol-targeting pressures, remodeling of the ergosterol biosynthetic pathway through altered *ERG11* expression or coordinated changes in other sterol enzymes could provide a physiological advantage by maintaining membrane integrity or reducing drug susceptibility. In such scenarios, increased ergosterol production or altered sterol homeostasis may reflect adaptation to environmental stress rather than traits

selected within mammalian hosts. Our findings raise the possibility that metabolic adjustments that enhance tolerance to sterol-targeting pressures could also influence host–pathogen interactions, such that the heightened virulence observed in some isolates represents a collateral consequence of environmental metabolic adaptation.

This framework contrasts with classic examples in which resistance-associated mutations impose fitness costs. In *Candida albicans*, gain-of-function mutations in the sterol regulator UPC2 often enhance azole resistance but can attenuate virulence in drug-free contexts[57,58]. In contrast, the *F. oxysporum* clinical isolates examined here exhibit reduced azole susceptibility without an apparent fitness compromise in our in vivo models. One possible explanation is that increased ergosterol flux simultaneously stabilizes membrane integrity under stress while generating extracellular sterols capable of modulating host immune responses.

Therapeutically, these findings suggest that management of invasive fusariosis may require approaches beyond antifungal monotherapy. If disease severity reflects ergosterol-driven pyroptosis and chemokine paralysis, then host-directed interventions could complement antifungal treatment. Pharmacologic modulation of inflammasome signaling, including NLRP3 inhibitors currently under clinical investigation for autoinflammatory diseases[59], caspase-1 inhibitors such as VX-765[60], or emerging strategies targeting gasdermin-mediated pore formation[61], could, in principle, preserve macrophage viability and prevent excessive pyroptosis during early infection. Likewise, targeting immunoregulatory circuits that suppress chemokines, including *IL-10* or *TGF-β* signaling pathways, might restore neutrophil recruitment. Several biologics that interfere with *IL-10* or *TGF-β* signaling are already in clinical development for other indications, suggesting translational feasibility[62,63]. Conversely, agents that enhance neutrophil trafficking or function, including G-CSF or GM-CSF, may help counteract chemokine suppression in selected patients[64,65]. Careful balancing would be required to avoid exacerbating tissue-damaging inflammation, but the concept of interrupting the metabolic–immune axis opens new therapeutic avenues. Beyond host-directed immunomodulation, our findings raise important considerations for antifungal therapy. Azole drugs target Erg11 and induce compensatory upregulation of sterol biosynthetic pathways via Upc2-dependent mechanisms[66,67]. It is therefore conceivable that suboptimal azole exposure during active infection could enhance sterol flux and potentially amplify ergosterol-mediated immunopathology. Although this hypothesis requires

direct experimental validation, it underscores the importance of optimized dosing strategies and raises the possibility that antifungal classes that do not stimulate compensatory sterol upregulation may have distinct immunological consequences. In addition, the sterol secretion profile and baseline activation state of sterol biosynthetic regulators such as Upc2 may represent candidate biomarkers of virulence potential. Stratifying clinical isolates by ergosterol flux or sterol transcriptional activity could, in principle, identify strains with heightened immunopathogenic capacity and inform risk assessment in vulnerable patients.

Finally, our study reframes ergosterol from a static membrane component and antifungal target into an active determinant of host–pathogen interaction. Variation in sterol biosynthesis among *F. oxysporum* isolates can generate a metabolic state that simultaneously reduces azole susceptibility and reshapes innate immunity. This sterol-remodeled phenotype promotes macrophage pyroptosis, suppresses chemokine-mediated recruitment through *IL-10*/*TGF-β*–linked mechanisms, and may facilitate fungal persistence in immunocompromised hosts. More broadly, these findings highlight how variation in core metabolic pathways can influence host–pathogen interactions in opportunistic fungi. Understanding the ecological contexts in which such metabolic states arise may therefore be as important as dissecting classical virulence factors when considering the emergence of cross-kingdom fungal strains with increased pathogenic potential.

Methods

Fungal strains and growth conditions

A list of fungal strains used in this study is provided in Supplementary Table 1. Environmental *F. oxysporum* isolates were sampled from soil in Germany, while clinical isolates were obtained from the German National Reference Center for Invasive Fungal Infections (NRZMyk). All isolates were subjected to molecular species identification. The conidia of the fungal strains were stored at -80 °C in an ultra-freezer in 25% glycerol (v/v) for long-term storage, and the strains were propagated from their stocks on Potato Dextrose Agar (PDB, BD Difco™, USA) at 28 °C for at least 4 days. The conidia were collected using PBS. The spore concentrations were determined using a hemocytometer.

800 ***Susceptibility assay for cell wall and membrane stress***

801 To monitor growth under antifungal drugs, 1×10^4 conidia were spotted onto agar plates that were
802 supplemented with varying concentrations of fluconazole (FLUC), voriconazole (VCRZ) and
803 amphotericin B (AMPHO), The plates were incubated for 3 days at 28 °C, and the extent of
804 vegetative growth was used as a relative indicator of sensitivity.
805
806 ***Culturing and preparation of the PBMC macrophages***

807 Human blood was obtained from healthy volunteers, with informed consent, in compliance with
808 the guidelines of the Hebrew University of Jerusalem Research Ethics Committee. Human
809 neutrophils were collected and were maintained as previously described[68] and used for the cell
810 damage assay (LDH release) and Rt-qPCR analyses.

811 ***Mouse model of systemic fusariosis***

812 The animal infection was performed according to Schäfer et. al[69]. Immunosuppressed mice were
813 challenged intravenously with *F. oxysporum* conidia via lateral tail vein injection (0.2 mL
814 inoculum; 2×10^6 conidia per mouse). Immunosuppression was induced with cyclophosphamide
815 (150 mg kg^{-1}, intraperitoneal) on day 0 and repeated every 3 days thereafter, as previously
816 described[69]. Animals were monitored for up to 10 days post-challenge and euthanized at
817 predefined endpoints, including severe clinical signs and/or >20% loss of initial body weight.
818 Survival data were plotted as Kaplan–Meier curves and compared using the log-rank (Mantel–
819 Cox) test in GraphPad Prism 8.

820 ***Protein extraction and western blot assay***

821 To determine the cleaved GSDMD expression levels, conidia (2×10^6) of the *F. oxysporum*
822 strains were inoculated in 24 wells plate together to human PBMC 37 °C for 6 h. For PBMCs
823 cells protein extraction, 0.5 mL RIPA buffer containing 1 mM PMSF and protease inhibitor was
824 added to the PBMS cells, the cells were transferred to 2 mL tubes containing glass beads, and
825 then the cells were mixed using a mechanical incubation for 5 min (10 cycles 30 sec each,
826 followed by 2 min on ice after each cycle). Extracts were centrifuged at 20,000×g for 40 minutes
827 at 4 °C. The supernatants were collected, and the protein concentrations were determined using

828 the Bradford method. 30 µg of protein from each sample were resolved in a 12% (w/v) SDS–
829 PAGE and transferred to nitrocellulose membranes (BioRad). Cleaved GSDMD was examined
830 using anti-GSDMD / GSDMDD (Full Length+N terminal – Abclonal ABC-A20197) anti-Rabbit
831 pAb (ABclonal ABC-A20197), following the manufacturer's instructions using a 1:1000 dilution
832 in TBST buffer (137 mM NaCl, 20 mM Tris, 0.1% Tween-20) containing 5% (w/v) BSA and 16
833 h incubation at 4 °C. Primary antibody was detected using an HRP-conjugated secondary
834 antibody raised in rabbit for GSDMD and an HRP-conjugated secondary antibody raised in
835 rabbit for IL-18. Anti-histone H-1 (sc-393358; Santa Cruz Biotechnology) was used as a loading
836 control in the experiments. Incubation was performed at 1:2000 dilution in TBST containing 5%
837 (w/v) BSA, with rocking on a platform for 16 hours at 4 °C. Chemoluminescent detection was
838 achieved by using ECL Prime Western Blot detection kit (GE HealthCare). Images were
839 generated by exposing the membranes to the ChemiDoc XRS gel imaging system (BioRad). The
840 images were subjected to densitometric analysis using ImageJ software[70].

841 ***In-solution caspase activity assay***

842 Caspase-1 and Caspase-1/4 activity was quantified using a commercial fluorometric assay
843 following the manufacturer's instructions (Santa Cruz Biotechnology, sc-311280, sc-311282).
844 Briefly, PBMCs were incubated with *F. oxysporum* strains for the indicated times in black, flat-
845 bottom 96-well plates compatible with fluorescence detection. For each well, 50 µl of cell
846 culture was mixed with 200 µl of caspase reaction buffer (50 mM HEPES, pH 7.4; 100 mM
847 NaCl; 1 mM EDTA; 10 mM DTT) supplemented with 50 µM fluorogenic AFC-conjugated
848 substrate. Reactions were incubated for 2 h at 37 °C protected from light, and AFC release was
849 measured on a microplate reader (excitation 400 nm; emission 505 nm). Raw fluorescence values
850 were corrected by subtracting medium-only background and then normalized to untreated PBMC
851 controls. Caspase activity is reported as fold change relative to untreated cells.

852 ***Human-derived macrophages cell damage assay (LDH release)***

853 Human PBMC damage was quantified by measuring lactate dehydrogenase (LDH) released into
854 the culture supernatant. using the CytoTox 96(R) Non-Radio. Cytotoxicity Assay (Promega,
855 G1780), according to the manufacturer's protocol. Spontaneous LDH release (negative control)
856 was assessed from 5×10^5 PBMCs cultured in medium alone for 6 h at 37 °C with 5% CO_2.

Maximum LDH release (positive control) was obtained by lysing 5×10^5 PBMCs with kit lysis buffer under the same conditions. Percent cytotoxicity was calculated relative to the maximum-release condition, which was defined as 100% cell death[71].

Fungal burden

The fungal burden in the organs was assessed using two approaches: (1) measurement of colony-forming units (CFU) by plating and (2) quantification of fungal DNA levels in each organ using real-time PCR using the translation elongation factor 1-α (*EF1α*)[72] . To determine the CFU, the organs were lysed, and the lysates were then serially diluted and plated onto potato dextrose agar (PDA). After an incubation period, the resulting fungal colonies were counted, and the CFU values were determined.

Ergosterol quantification using flow cytometry

Filipin, a fluorescent polyene antibiotic that binds sterols, was used to evaluate sterol distribution in the germlings[73]. Briefly, the conidia were germinated for 4 hours at 28 ºC. After incubation, they were centrifuged, resuspended in 1x PBS, and then 15 ug/mL of filipin was added. The conidia were incubated for 10 minutes at 28 °C, washed 3 times with PBS, and resuspended in PBS. The Filipin level was quantified by flow cytometry using a NovoCyte Quanteon Flow Cytometer using a Pacific blue filter (452 nm).

Supernatant ergosterol quantification

Sterol extraction and GC–MS analysis. Fungal strains were cultured in liquid Czapek–Dox medium under the indicated conditions after inoculation with 1×10^6 spores. For the Ergosterol extraction, culture supernatants were harvested by Miracloth filtration to remove fungal biomass, then centrifuged at 4,000*g* for 10 min to remove residual cells and debris. Clarified supernatants were then subjected to sterol extraction using freshly prepared Mandala buffer (42% ethanol, 14% diethyl ether, 3% pyridine, and 0.05% NH_4OH), with Epi-cholesterol added at the start of the procedure as an internal standard[73]. Extracts were analyzed by GC–MS, and sterols were identified by spectral matching to a pure ergosterol standard (TCI). Relative abundance was calculated from integrated peak areas normalized to the Epi-cholesterol internal standard.

Total lipids extraction

Lipids were extracted from the culture supernatants of filtered *F. oxysporum isolates* using a modified Bligh and Dyer method[74]. Briefly, strains were grown in Czapek-Dox media at 28 °C with shaking (180 rpm.), after which the cultures were centrifuged at 3,000*g* for 10 min, and the supernatants were filtered to remove residual fungal material. The supernatant was subjected to biphasic extraction with methanol, chloroform, and water. Following centrifugation (2,000*g,* 5 min), the lower organic phase was collected into pre-weighed Eppendorf tubes and dried completely at 40 °C under a fume hood. Total lipid content was then determined gravimetrically by weighing the dried extract and subtracting the weight of the empty tube.

Histology analysis

After 5 days of *F. oxysporum* infection, the mice were euthanized by a recommended method. The kidneys, liver, spleen, and heart were surgically removed from each mouse. The collected organs were immediately fixed in 10% (v/v) neutral buffered formalin (pH 7.4) for 24 h. Following fixation, the organs were processed for paraffin embedding. Briefly, the tissues were dehydrated using a series of graded ethanol solutions, cleared in xylene, and infiltrated with molten paraffin wax. The tissues were then embedded in paraffin blocks. Paraffin-embedded tissue blocks were sectioned at a 4-6 μm thickness using a microtome. The tissue sections were mounted on glass slides, dried, and then subjected to routine hematoxylin and eosin (H&E) staining for histological analysis. The H&E-stained sections were examined under a light microscope with a high-resolution camera. Photomicrographs were captured to document the histopathological changes in the kidneys, liver, spleen, and heart.

Immunostaining with MPO

The spleen immunostaining for MPO detection followed the MIBI Assay Guide protocol. Deparaffinization and rehydration were performed by placing the slides in a slide rack and subjecting them to 20 min of incubation at 70 °C in an incubator or oven. Following heat removal, the slides were washed using the following agitation-based buffers: xylene (2 times for

30 seconds each), 100% (v/v) reagent alcohol (2 times for 30 sec each), 95% (v/v) reagent alcohol (2 times for 30 sec each), 80% (v/v) reagent alcohol (30 sec), 70% (v/v) reagent alcohol (30 seconds), and deionized water (2 times for 30 sec each). The Heat-induced Epitope Retrieval (HIER) step involved placing the slides in a preheated slide chamber containing 1x HIER buffer within a heat bath. Incubation was carried out at 97 °C for 40 minutes, followed by cooling to 65 °C for 30 minutes. The slide chamber was removed from the bath and allowed to rest at room temperature for 30 min. Subsequently, antibody blocking was performed by applying the blocking buffer onto the slides and incubating them at room temperature for 20 min. Primary antibody dilutions were prepared in blocking buffer and applied to the slides, which were then placed in a controlled humidified chamber overnight at 4 °C. On a subsequent day, the slides were subjected to a 2-h incubation at room temperature with the secondary antibody for MPO staining.

Quantitation of cytokine and chemokine transcripts by real-time RT-PCR

The expression levels of pro-inflammatory cytokines and chemokines were determined by Real-time RT-qPCR assays[75]. Briefly, PBMCs (2×10^6 in 24-well plates) were infected with *F. oxysporum* strains or (MOI = 5) for 3 and 6 h, respectively, and flash-frozen in liquid nitrogen. Total RNA was extracted using NucleoSpin RNA XS (MACHEREY-NAGEL) according to the manufacturer's directions and stored at −80 °C. Samples were reverse transcribed with the qScript cDNA Synthesis Kit (Quantabio). The primers for the individual genes were designed using Primer Express 3.0 software (Life Technologies) and are listed in Table S2. qRT-PCR was performed in duplicate with six independent biological samples in a StepOne Plus Real-Time PCR System (Thermo Scientific). Each primer pair's concentration was optimized before the efficiency curve reaction. According to the reference, only primers with amplification efficiency ranging from 5–105% were used[76]. No template controls (NTC) were used to confirm eliminating contaminating DNA in every run. A melt curve analysis was performed after the PCR was complete to confirm the absence of nonspecific amplification products. The fold change in mRNA abundance was calculted using $2-\Delta\Delta Ct$[75], and all the values were normalized to the expression of *GAPDH*.

Detection of proinflammatory cytokines and chemokines by enzyme-linked immunosorbent assay (ELISA)

For the detection of proinflammatory cytokines and chemokines such as *IL-1β*, *IL-6*, *TNF-α*, *CXCL1*, and *CXCL2* in macrophage culture supernatants, PBMCs from human blood (2×10^6 cells/well in 48-well plates) were infected with PBS or *F. oxysporum* strain cells (MOI = 5) for the time indicated above. After treatment, supernatants were collected and stored at −80 °C until analysis and cytokine/chemokine production in supernatant was measured by ELISA with ELISA kits according to the manufacturer's recommendations (eBioscience and R&D Systems).

Flow cytometry

Single-cell suspensions from mouse kidney and spleen were generated using mechanical and enzymatic dissociation. Briefly, tissues were minced and digested in RPMI (or PBS, as appropriate) containing collagenase IV (1 mg mL^{-1}) and DNase I (0.1 mg mL^{-1}) for 40 min at 37 °C, followed by further dissociation using a gentleMACS™ Dissociator (Miltenyi Biotec). Cell suspensions were filtered through a 40-µm cell strainer to obtain single-cell preparations. Prior to staining, cells were incubated with anti-mouse CD16/CD32 Fc block in PBS supplemented with 5% (v/v) fetal bovine serum (FBS) for 30 min at 4 °C, washed with PBS/5% (v/v) FBS, and then stained with the indicated antibody to identify immune cell populations.

Fluorescence Probe Assay for Fluconazole Uptake

Conidia of *F. oxysporum* strains Fol4287, MRL8996, and NRRL32931 were germinated in PDB at 28 °C until swollen conidia (for flow cytometry) and short hyphae (for microscopy) were observed. A fluorescent azole probe was diluted immediately before use in the corresponding culture medium and added to the fungal suspension at a 1:1 ratio to yield a final concentration of 1 µM. After incubation for 2 hours in the dark, samples were counterstained with SYTO 9 and examined by fluorescence microscopy. Probe-derived fluorescence was collected in the DAPI channel, whereas SYTO 9 signal was collected in the GFP channel. Images were acquired using identical microscope settings across strains to allow qualitative comparison of probe uptake.

NF-κB Inhibition Assay in Ergosterol-Stimulated Human PBMC-derived macrophages

Human PBMC-derived macrophages were first pretreated for 1 h with BAY 11-7082 (5 μM) or DMSO for a no-treatment control, followed by stimulation with the indicated concentrations of ergosterol for 6 h. Total RNA was extracted, quantified, and reverse-transcribed to cDNA. Transcript levels were measured by RT–qPCR using *GAPDH* as the endogenous control, and relative gene expression was calculated using the $2^{-\Delta\Delta ct}$ method[74].

RNA-seq analysis

RNA-seq datasets were obtained from the NCBI Sequence Read Archive (SRA) under accession numbers PRJNA1393456 and PRJNA1395065. Samples from wild-type *F. oxysporum* strains NRRL32931, MRL8996, and Fol4287 grown in YPD medium at pH 5 or pH 7.4 were included in the present analysis. Raw reads were processed using Trimmomatic v0.32[77] for adapter removal and quality trimming, and the resulting reads were aligned to the corresponding reference genomes NRL32931 and MRL8996 or Fol4287 using HISAT2 v2.0.5[78]. Gene-level expression was quantified using StringTie v1.30[79]. Normalized expression values were scaled to the housekeeping gene *ACT* for descriptive visualization of genes in the ergosterol biosynthesis pathway.

Acknowledgments

We thank Dr. Grit Walther and the National Reference Center for Invasive Fungal Infections for molecular species identification and sharing of the clinical *F. oxysporum* isolates.

Funding

The work in N.S.'s lab was funded by Israeli Science Foundation (ISF) grants 3021/20 and 1760/20. The work in S.J.'s lab is supported by the Free State of Thuringia and the European Social Fund Plus (projects FusInfect 2022FGR0007, and FUSION 2025FGR0025), as well as the BMFTR funding program Photonics Research Germany ("LPI-BT2-IPHT", FKZ 13N15704) which is integrated into the Leibniz Center for Photonics in Infection Research (LPI).

Author Contributions Statement

M.C.R. conceived the study, designed and performed experiments, analyzed the data, and wrote

the manuscript. J.A., H.H., M.W., E.G. and S.J. performed experiments, analyzed the data and reviewed the manuscript. E.S.O. analyzed the data and reviewed the manuscript. J.J.C. and L.-J.M. contributed to the conceptual development of the study and reviewed and edited the manuscript. N.S. conceived and supervised the study, acquired funding, and reviewed and edited the manuscript.

Competing Interests Statement

The authors declare no competing interests.

References

1. Bongomin, F., Gago, S., Oladele, R. O. & Denning, D. W. Global and Multi-National Prevalence of Fungal Diseases-Estimate Precision. *J. Fungi Basel Switz.* **3**, (2017).
2. Sharma, K. *et al.* Exserohilum rostratum: Characterization of a Cross-Kingdom Pathogen of Plants and Humans. *PLOS ONE* **9**, e108691 (2014).
3. van Baarlen, P., van Belkum, A., Summerbell, R. C., Crous, P. W. & Thomma, B. P. H. J. Molecular mechanisms of pathogenicity: how do pathogenic microorganisms develop cross-kingdom host jumps? *FEMS Microbiol. Rev.* **31**, 239–277 (2007).
4. Acosta-España, J. D., Evangelista, A. J. de J., de Oliveira, J. S. & Serpa, R. Editorial: Fungal virulence. *Front. Fungal Biol.* **Volume 5-2024**, (2025).
5. Casadevall, A., Steenbergen, J. N. & Nosanchuk, J. D. 'Ready made' virulence and 'dual use' virulence factors in pathogenic environmental fungi — the Cryptococcus neoformans paradigm. *Curr. Opin. Microbiol.* **6**, 332–337 (2003).
6. Denning, D. W. Global incidence and mortality of severe fungal disease. *Lancet Infect. Dis.* **24**, e428–e438 (2024).
7. Casalini, G., Giacomelli, A. & Antinori, S. The WHO fungal priority pathogens list: a crucial reappraisal to review the prioritisation. *Lancet Microbe* **5**, 717–724 (2024).
8. *WHO Fungal Priority Pathogens List to Guide Research, Development and Public Health Action*. (World Health Organization, Geneva, 2022).
9. Ma, L.-J. *et al.* Comparative genomics reveals mobile pathogenicity chromosomes in Fusarium. *Nature* **464**, 367–373 (2010).
10. Nucci, M. & Anaissie, E. Invasive fusariosis. *Clin. Microbiol. Rev.* **36**, e0015922 (2023).
11. Ferreira da Cunha Neto, J. *et al.* Fusarioid keratitis and other superficial infections: A 10-years prospective study from Northeastern Brazil. *PLoS Negl. Trop. Dis.* **18**, e0012247 (2024).
12. Sáenz, V. *et al.* A One Health Perspective to Recognize Fusarium as Important in Clinical Practice. *J. Fungi Basel Switz.* **6**, (2020).
13. Nucci, M. & Anaissie, E. Fusarium infections in immunocompromised patients. *Clin. Microbiol. Rev.* **20**, 695–704 (2007).
14. Fisher, M. C. & Denning, D. W. The WHO fungal priority pathogens list as a game-changer. *Nat. Rev. Microbiol.* **21**, 211–212 (2023).

15. Hassan, A. S. *et al.* Antifungal Susceptibility and Phylogeny of Opportunistic Members of the Genus Fusarium Causing Human Keratomycosis in South India. *Med. Mycol.* **54**, 287–294 (2016).
16. Fisher, M. C., Hawkins, N. J., Sanglard, D. & Gurr, S. J. Worldwide emergence of resistance to antifungal drugs challenges human health and food security. *Science* **360**, 739–742 (2018).
17. Applebach, E. *et al.* Prevalence and diversity of antifungal resistance in *Fusarium* isolates across clinical and agricultural settings in the United States. *Antimicrob. Agents Chemother.* **69**, e01208-25 (2025).
18. Money, N. P. Fungal thermotolerance revisited and why climate change is unlikely to be supercharging pathogenic fungi (yet). *Fungal Biol.* **128**, 1638–1641 (2024).
19. Janeway CA Jr. *Immunobiology: The Immune System in Health and Disease. 5th Edition.* (2001).
20. Sperandio, B., Fischer, N. & Sansonetti, P. J. Mucosal physical and chemical innate barriers: Lessons from microbial evasion strategies. *What Pathog. Teach Us Immune Syst.* **27**, 111–118 (2015).
21. Uribe-Querol, E. & Rosales, C. Control of Phagocytosis by Microbial Pathogens. *Front. Immunol.* **Volume 8-2017**, (2017).
22. Murdoch, C. C. & Skaar, E. P. Nutritional immunity: the battle for nutrient metals at the host–pathogen interface. *Nat. Rev. Microbiol.* **20**, 657–670 (2022).
23. Silva, M. T. When two is better than one: macrophages and neutrophils work in concert in innate immunity as complementary and cooperative partners of a myeloid phagocyte system. *J. Leukoc. Biol.* **87**, 93–106 (2010).
24. Ayhan Dilay Hazal *et al.* Host-specific adaptation in Fusarium oxysporum correlates with distinct accessory chromosome content in human and plant pathogenic strains. *mBio* **16**, e00951-25 (2025).
25. Briard, B., Malireddi, R. K. S. & Kanneganti, T.-D. Role of inflammasomes/pyroptosis and PANoptosis during fungal infection. *PLOS Pathog.* **17**, e1009358 (2021).
26. Swanson, K. V., Deng, M. & Ting, J. P.-Y. The NLRP3 inflammasome: molecular activation and regulation to therapeutics. *Nat. Rev. Immunol.* **19**, 477–489 (2019).
27. Bruna Gerardon Batista, A. M. F. Human fusariosis: An emerging infection that is difficult to treat. *Rev Soc Bras Med Trop* https://doi.org/10.1590/0037-8682-0013-2020 (2020) doi:10.1590/0037-8682-0013-2020.
28. Zhang, Y. *et al.* The genome of opportunistic fungal pathogen Fusarium oxysporum carries a unique set of lineage-specific chromosomes. *Commun. Biol.* **3**, 50 (2020).
29. Yu, H. *et al.* Conservation and Expansion of Transcriptional Factor Repertoire in the Fusarium oxysporum Species Complex. *J. Fungi* **9**, 359 (2023).
30. Ayhan, D. H., López-Díaz, C., Di Pietro, A. & Ma, L.-J. Improved Assembly of Reference Genome Fusarium oxysporum f. sp. lycopersici Strain Fol4287. *Microbiol. Resour. Announc.* **7**, (2018).
31. Fan, Y. *et al.* Skin Microvascular Thrombosis in Fusarium Infection in Two Early Biopsied Cases. *Case Rep. Dermatol.* **2**, 76–81 (2010).
32. Lionakis, M. S., Drummond, R. A. & Hohl, T. M. Immune responses to human fungal pathogens and therapeutic prospects. *Nat. Rev. Immunol.* **23**, 433–452 (2023).

33. Taylor, A., Verhagen, J., Blaser, K., Akdis, M. & Akdis, C. A. Mechanisms of immune suppression by interleukin-10 and transforming growth factor-β: the role of T regulatory cells. *Immunology* **117**, 433–442 (2006).
34. Del Sero, G. *et al.* Antifungal type 1 responses are upregulated in IL-10-deficient mice. *Microbes Infect.* **1**, 1169–1180 (1999).
35. Dai, Y., Datta, S., Novotny, M. & Hamilton, T. A. TGFβ inhibits LPS-induced chemokine mRNA stabilization. *Blood* **102**, 1178–1185 (2003).
36. Schroder, K. & Tschopp, J. The inflammasomes. *Cell* **140**, 821–832 (2010).
37. Shi, J. *et al.* Cleavage of GSDMD by inflammatory caspases determines pyroptotic cell death. *Nature* **526**, 660–665 (2015).
38. Liu, X. *et al.* Inflammasome-activated gasdermin D causes pyroptosis by forming membrane pores. *Nature* **535**, 153–158 (2016).
39. Wu, Y. *et al.* Cell pyroptosis in health and inflammatory diseases. *Cell Death Discov.* **8**, 191 (2022).
40. Uwamahoro Nathalie *et al.* The Pathogen Candida albicans Hijacks Pyroptosis for Escape from Macrophages. *mBio* **5**, 10.1128/mbio.00003-14 (2014).
41. Wellington, M., Koselny, K., Sutterwala, F. S. & Krysan, D. J. Candida albicans triggers NLRP3-mediated pyroptosis in macrophages. *Eukaryot. Cell* **13**, 329–340 (2014).
42. Benhamou, R. I. *et al.* Real-Time Imaging of the Azole Class of Antifungal Drugs in Live Candida Cells. *ACS Chem. Biol.* **12**, 1769–1777 (2017).
43. Campoli, P. *et al.* Pharmacokinetics of posaconazole within epithelial cells and fungi: insights into potential mechanisms of action during treatment and prophylaxis. *J. Infect. Dis.* **208**, 1717–1728 (2013).
44. Vallejo, M. C. *et al.* Lipidomic Analysis of Extracellular Vesicles from the Pathogenic Phase of Paracoccidioides brasiliensis. *PLOS ONE* **7**, e39463 (2012).
45. Maximo, M. F., Fill, T. P. & Rodrigues, M. L. A Close Look into the Composition and Functions of Fungal Extracellular Vesicles Produced by Phytopathogens. *Mol. Plant-Microbe Interactions®* **36**, 228–234 (2023).
46. Rajamäki, K. *et al.* Cholesterol Crystals Activate the NLRP3 Inflammasome in Human Macrophages: A Novel Link between Cholesterol Metabolism and Inflammation. *PLOS ONE* **5**, e11765 (2010).
47. Tall, A. R. & Yvan-Charvet, L. Cholesterol, inflammation and innate immunity. *Nat. Rev. Immunol.* **15**, 104–116 (2015).
48. Koselny Kristy *et al.* A Genome-Wide Screen of Deletion Mutants in the Filamentous Saccharomyces cerevisiae Background Identifies Ergosterol as a Direct Trigger of Macrophage Pyroptosis. *mBio* **9**, 10.1128/mbio.01204-18 (2018).
49. Sanjabi, S., Zenewicz, L. A., Kamanaka, M. & Flavell, R. A. Anti-inflammatory and pro-inflammatory roles of TGF-β, IL-10, and IL-22 in immunity and autoimmunity. *Cancer/Immunomodulation* **9**, 447–453 (2009).
50. Li, M. O. & Flavell, R. A. Contextual Regulation of Inflammation: A Duet by Transforming Growth Factor-β and Interleukin-10. *Immunity* **28**, 468–476 (2008).
51. Vagima, Y. *et al.* Circumventing Y. pestis Virulence by Early Recruitment of Neutrophils to the Lungs during Pneumonic Plague. *PLOS Pathog.* **11**, e1004893 (2015).

52. Doganyigit, Z., Eroglu, E. & Akyuz, E. Inflammatory mediators of cytokines and chemokines in sepsis: From bench to bedside. *Hum. Exp. Toxicol.* **41**, 09603271221078871 (2022).
53. Karmakar, M., Katsnelson, M. A., Dubyak, G. R. & Pearlman, E. Neutrophil P2X7 receptors mediate NLRP3 inflammasome-dependent IL-1β secretion in response to ATP. *Nat. Commun.* **7**, 10555 (2016).
54. Yalcinkaya, M. & Tall, A. R. Cholesterol Crystals as Triggers of NLRP3 Inflammasome Activation in Atherosclerosis. *Curr. Atheroscler. Rep.* **27**, 77 (2025).
55. Kuroda, E., Sugiura, T., Okada, K., Zeki, K. & Yamashita, U. Prostaglandin E2 Up-Regulates Macrophage-Derived Chemokine Production but Suppresses IFN-Inducible Protein-10 Production by APC1. *J. Immunol.* **166**, 1650–1658 (2001).
56. Applebach Emilie *et al.* Prevalence and diversity of antifungal resistance in Fusarium isolates across clinical and agricultural settings in the United States. *Antimicrob. Agents Chemother.* **69**, e01208-25 (2025).
57. Flowers Stephanie A. *et al.* Gain-of-Function Mutations in UPC2 Are a Frequent Cause of ERG11 Upregulation in Azole-Resistant Clinical Isolates of Candida albicans. *Eukaryot. Cell* **11**, 1289–1299 (2012).
58. Lohberger, A., Coste, A. T. & Sanglard, D. Distinct roles of Candida albicans drug resistance transcription factors TAC1, MRR1, and UPC2 in virulence. *Eukaryot. Cell* **13**, 127–142 (2014).
59. Cabral, J. E. *et al.* Targeting the NLRP3 inflammasome for inflammatory disease therapy. *Trends Pharmacol. Sci.* **46**, 503–519 (2025).
60. Amand, M. *et al.* The anti-caspase 1 inhibitor VX-765 reduces immune activation, CD4+ T cell depletion, viral load, and total HIV-1 DNA in HIV-1 infected humanized mice. *eLife* **12**, e83207 (2023).
61. Kopp, A. *et al.* Pyroptosis inhibiting nanobodies block Gasdermin D pore formation. *Nat. Commun.* **14**, 7923 (2023).
62. Jing, H., Gao, Y., Jing, L., Yang, H. & Liu, S. Recent advances in therapeutic use of transforming growth factor-beta inhibitors in cancer and fibrosis. *Front. Oncol.* **Volume 15-2025**, (2025).
63. Wyatt, N. J., Speight, R. A., Stewart, C. J., Kirby, J. A. & Lamb, C. A. Targeting Leukocyte Trafficking in Inflammatory Bowel Disease. *BioDrugs* **35**, 473–503 (2021).
64. Yong, K. Granulocyte colony-stimulating factor (G-CSF) increases neutrophil migration across vascular endothelium independent of an effect on adhesion: comparison with granulocyte-macrophage colony-stimulating factor (GM-CSF). *Br. J. Haematol.* **94**, 40–47 (1996).
65. Pinder, E. M. *et al.* Randomised controlled trial of GM-CSF in critically ill patients with impaired neutrophil phagocytosis. *Thorax* **73**, 918–925 (2018).
66. Moye-Rowley, W. S. Linkage between genes involved in azole resistance and ergosterol biosynthesis. *PLOS Pathog.* **16**, e1008819 (2020).
67. Song Jia L., Harry Jo Beth, Eastman Richard T., Oliver Brian G., & White Theodore C. The Candida albicans Lanosterol 14-α-Demethylase (ERG11) Gene Promoter Is Maximally Induced after Prolonged Growth with Antifungal Drugs. *Antimicrob. Agents Chemother.* **48**, 1136–1144 (2004).

68. Rocha, M. C. *et al.* Aspergillus fumigatus dsRNA virus promotes fungal fitness and pathogenicity in the mammalian host. *Nat. Microbiol.* https://doi.org/10.1038/s41564-025-02096-3 (2025) doi:10.1038/s41564-025-02096-3.
69. Schäfer, K., Di Pietro, A., Gow, N. A. R. & MacCallum, D. Murine Model for Fusarium oxysporum Invasive Fusariosis Reveals Organ-Specific Structures for Dissemination and Long-Term Persistence. *PLOS ONE* **9**, e89920 (2014).
70. Schindelin, J. *et al.* Fiji: an open-source platform for biological-image analysis. *Nat. Methods* **9**, 676–682 (2012).
71. Ding, X. *et al.* Inflammasome-mediated GSDMD activation facilitates escape of Candida albicans from macrophages. *Nat. Commun.* **12**, 6699 (2021).
72. Cobo-Díaz, J. F., Baroncelli, R., Le Floch, G. & Picot, A. A novel metabarcoding approach to investigate Fusarium species composition in soil and plant samples. *FEMS Microbiol. Ecol.* **95**, fiz084 (2019).
73. Fabri, J. H. T. M. *et al.* The AGC Kinase YpkA Regulates Sphingolipids Biosynthesis and Physically Interacts With SakA MAP Kinase in Aspergillus fumigatus. *Front. Microbiol.* **Volume 9-2018**, (2019).
74. BLIGH, E. G. & DYER, W. J. A rapid method of total lipid extraction and purification. *Can. J. Biochem. Physiol.* **37**, 911–917 (1959).
75. Livak, K. J. & Schmittgen, T. D. Analysis of relative gene expression data using real-time quantitative PCR and the 2(-Delta Delta C(T)) Method. *Methods San Diego Calif* **25**, 402–408 (2001).
76. Bustin, S. A. *et al.* The MIQE guidelines: minimum information for publication of quantitative real-time PCR experiments. *Clin. Chem.* **55**, 611–622 (2009).
77. Bolger, A. M., Lohse, M. & Usadel, B. Trimmomatic: a flexible trimmer for Illumina sequence data. *Bioinforma. Oxf. Engl.* **30**, 2114–2120 (2014).
78. Kim, D., Paggi, J. M., Park, C., Bennett, C. & Salzberg, S. L. Graph-based genome alignment and genotyping with HISAT2 and HISAT-genotype. *Nat. Biotechnol.* **37**, 907–915 (2019).
79. Pertea, M. *et al.* StringTie enables improved reconstruction of a transcriptome from RNA-seq reads. *Nat. Biotechnol.* **33**, 290–295 (2015).